Cone bipolar cell synapses generate transient versus sustained signals in parallel ON pathways of the mouse retina

Sidney P. Kuo[1,2], Wan-Qing Yu[3], Prerna Srivastava[4], Haruhisa Okawa[3], Luca Della Santina[3], David M. Berson[5], Gautam B. Awatramani[4], Rachel O.L. Wong[3], Fred Rieke[1]

[1]Department of Physiology and Biophysics, University of Washington, Seattle WA
[2]Department of Neuroscience, University of Minnesota, Minneapolis MN
[3]Department of Biological Structure, University of Washington, Seattle WA
[4]Department of Biology, University of Victoria, Victoria BC
[5]Department of Neuroscience, Brown University, Providence RI

Correspondence: Fred Rieke, rieke@uw.edu

Abstract

Parallel processing is a fundamental organizing principle in the nervous system, and understanding how parallel neural circuits generate distinct outputs from common inputs is a key goal of neuroscience. In the mammalian retina, divergence of cone signals into multiple feed-forward bipolar cell pathways forms the initial basis for parallel retinal circuits dedicated to specific visual functions. Here, we used patch-clamp electrophysiology, electron microscopy and two photon imaging of a fluorescent glutamate sensor to examine how kinetically distinct responses arise in transient versus sustained ON alpha RGCs (ON-T and ON-S RGCs) of the mouse retina. We directly compared the visual response properties of these RGCs with their presynaptic bipolar cell partners, which we identified using 3D electron microscopy reconstruction. Different ON bipolar cell subtypes (type 5i, type 6 and type 7) had indistinguishable light-driven responses whereas extracellular glutamate signals around RGC dendrites and postsynaptic excitatory currents measured in ON-T and ON-S RGCs in response to the identical stimuli used to probe bipolar cells were kinetically distinct. Anatomical examination of the bipolar cell axon terminals presynaptic to ON-T and ON-S RGCs suggests bipolar subtype-specific differences in the size of synaptic ribbon-associated vesicle pools may contribute to transient versus sustained kinetics. Our findings indicate bipolar cell synapses are a primary point of divergence in kinetically distinct visual pathways.

Introduction

Divergence into parallel pathways allows neural circuits to generate diverse outputs from a common set of inputs. This functional diversity can be quite striking; in vision, for example, light inputs initially encoded by the same collection of cone photoreceptors mediate sensitivity to several kinds of motion, to color and to spatial structure, all in the same region of space. These diverse functional sensitivities arise through parallel processing of light inputs, first in the retina and subsequently in downstream visual areas. Here we focus on the mechanisms producing transient and sustained responses – a key differentiating characteristic of retinal output cells across species (Baden et al., 2016; Bae et al., 2018; Cleland et al., 1973; Ikeda and Wright, 1972; Roska and Werblin, 2001; Werblin, 1970).

The retina provides a unique opportunity to study the mechanisms that differentiate signals in parallel pathways. We have a near-complete list of retinal cell types and substantial information about which of these cell types participate in specific parallel pathways (Helmstaedter et al., 2013; Masland, 2012). Under daylight conditions, retinal processing starts with cone photoreceptors transducing light inputs and providing divergent output to ~13 types of bipolar cell (Euler et al., 2014; Greene et al., 2016; Helmstaedter et al., 2013; Shekhar et al., 2016; Tsukamoto and Omi, 2017). The resulting bipolar cell signals are transmitted to ~20-40 retinal ganglion cell (RGC) types (Baden et al., 2016; Bae et al., 2018; Goetz et al., 2022). RGC inputs are strongly shaped by the activity of a large and diverse collection of amacrine cells that receive input from bipolar cells and provide presynaptic inhibition to bipolar cells and postsynaptic inhibition to RGCs (Diamond, 2017).

This circuitry produces highly distinct responses across RGC types - with cells that sample inputs on a variety of spatial and temporal scales, cells with distinct chromatic properties, cells that sense the direction of moving objects, and cells that separate local from global motion (Gollisch and Meister, 2010; Kerschensteiner, 2022). Several mechanisms contribute to these functional differences, starting with the division of signals into ON and OFF pathways at the cone-to-bipolar synapse (Euler et al., 2014; Slaughter and Miller, 1981). Temporal properties of responses of different bipolar cells can also differ for some stimuli (Awatramani and Slaughter,

2000; Baden et al., 2013; Euler et al., 2014; Euler and Masland, 2000; Ichinose et al., 2014; Ichinose and Hellmer, 2016; Wu et al., 2000). In the inner retina, integration of excitatory and inhibitory synaptic inputs produces directionally-selective responses in specific RGC types (Taylor and Vaney, 2002; Vaney et al., 2012) and differences in spatial weighting functions in other RGCs (Cafaro and Rieke, 2013; Roska and Werblin, 2001; Zhang et al., 2012). Properties of dendritic integration and RGC spike generation also differentiate responses of some RGCs (Margolis et al., 2010; Ran et al., 2020; Wienbar and Schwartz, 2022).

A fundamental difference among RGCs is whether their responses are sustained or transient (Baden et al., 2016; Bae et al., 2018; Cleland et al., 1973; Ikeda and Wright, 1972; Roska and Werblin, 2001). Cone photoreceptors respond to changes in light intensity with graded potentials that have both a transient and sustained component (Angueyra and Rieke, 2013; Cangiano et al., 2012; Szikra et al., 2014). Both kinetic components of the cone response are maintained in the firing rates of sustained cells, which track the prevailing contrast. However, only the initial component of the cone response is preserved in the spiking response of transient cells, which therefore respond primarily to changes in contrast. Where and how these differences originate is not clear. Here, we show that the distinct kinetics of responses of ON-sustained alpha and ON-transient alpha RGCs (1) persist for stimuli that elicit near-identical responses among the relevant bipolar cells, (2) do not depend on amacrine cell-mediated inhibition and, (3) are correlated with anatomical differences in output synapses of bipolar cell subtypes that are presynaptic to these RGCs. Together, these findings indicate that bipolar cell synapses are an important point of divergence in kinetically distinct visual pathways.

Results

We focused on two ON RGC cell types, ON-transient alpha (ON-T) and ON-sustained alpha (ON-S) RGCs, that could be readily identified in a flat-mount preparation of the isolated mouse retina (Fig. 1A) by their characteristic spiking response to a step increment in light intensity (Fig. 1B) (Bae et al., 2018; Goetz et al., 2022; Krieger et al., 2017; Kuo et al., 2016). Based on their light response, dendritic field size and stratification pattern in the inner plexiform layer (IPL) (see below; Fig. S4), the ON-T RGCs we studied here likely correspond to the 6sw RGC type of Bae et al. (2018) and the medium-field ON-transient RGC of Goetz et al. (2022).

We characterized the temporal spiking response properties of ON-T and ON-S RGCs by using an extracellular cell-attached patch electrode to measure action potential firing from either cell type while presenting a spatially uniform, randomly fluctuating light stimulus (Gaussian noise) that allowed us to efficiently probe a variety of stimulus contrasts and temporal frequencies. These and all subsequent physiological recordings were conducted using a photopic mean background light level (~3300 R*/rod/s; ~2000 P*/Scone/s) to suppress rod photoreceptor responses and therefore focus on cone-mediated signaling (Grimes et al., 2018; Ke et al., 2014). Figure 1C shows the spiking response of example ON-T and ON-S RGCs when we presented multiple repetitions of the same random stimulus contrast sequence; these RGC types clearly responded differently to temporally modulated light input. In particular, noise-evoked ON-T RGC spike responses were comprised primarily of large amplitude, less frequent spike bursts whereas ON-S RGC responses consisted of a more even distribution of small to large amplitude events (Fig. 1C and Fig S1A).

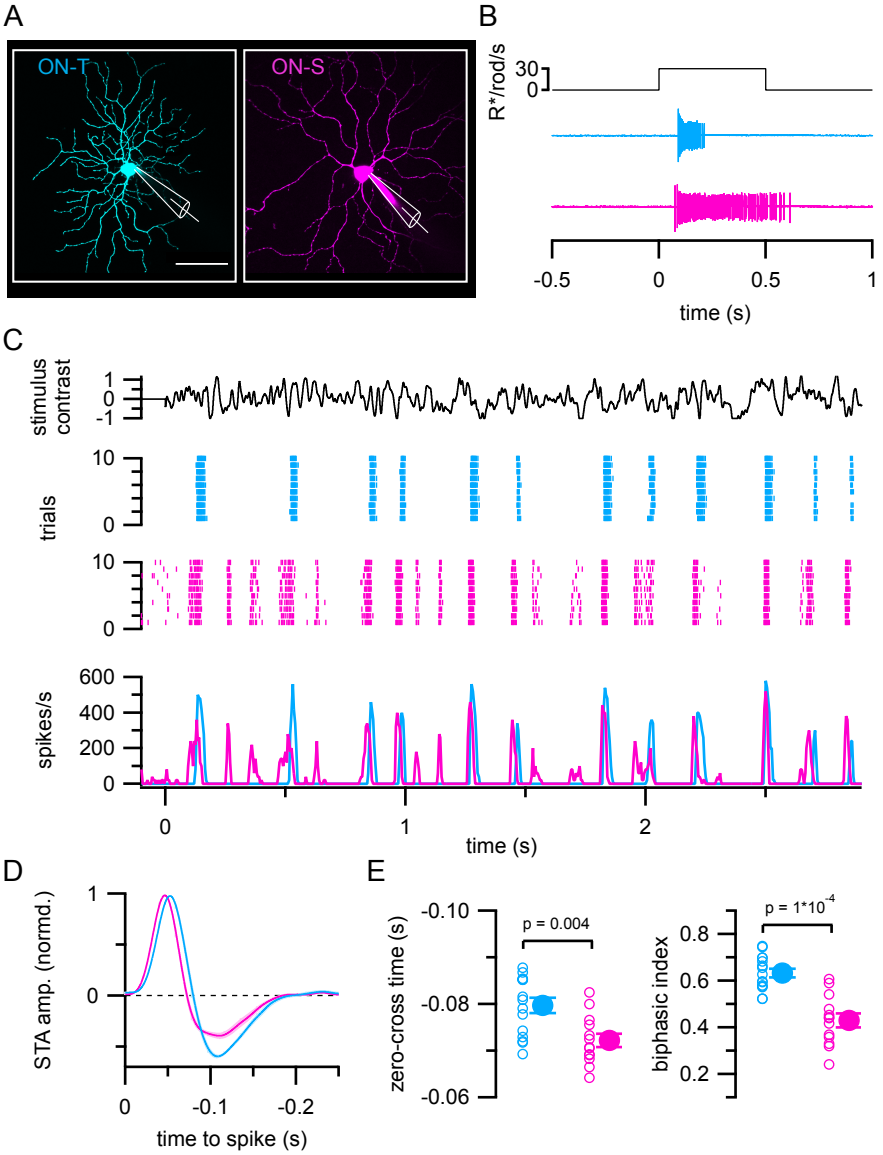

***Figure 1**. Distinct temporal spiking response properties of ON-transient versus ON-sustained RGCs. (A) Maximum intensity projection z-stack fluorescence images of ON-T (left, cyan) and ON-S (right, magenta) RGCs dialyzed with Alexa Fluor 594 during whole-cell patch-clamp recording. Scale bar 50 µm. (B) Characteristic spiking responses to light step increment of example ON-T and ON-S RGCs. (C) Example spiking responses to repeated trials of spatially uniform (300 µm spot diameter) Gaussian noise stimulus (top black trace) presented with a mean luminance of ~2400 P*/Scone/s (~3000 R*/rod/s). ON-T (cyan) and ON-S (magenta) RGCs were recorded from sequentially in the same piece of retina. PSTHs (bottom) calculated from 20 repetitions of noise stimulus. (D) ON-T and ON-S STAs derived from responses to non-repeated noise stimuli. Colored lines and shaded areas show mean ± SEM STA waveforms from ON-T (n= 15) and ON-S (n= 13) RGCs. Note time axis is reversed to facilitate comparison with linear filters in Figures 2 and 4. (E) Quantification of STA kinetics in different RGCs. Open circles show measurements from individual cells and filled circles with error bars show mean ± SEM values. Significance values from Wilcoxan rank sum tests.*

We summarized the response of each ON-T and ON-S RGC by computing the average stimulus preceding each recorded spike (the spike-triggered average or STA stimulus) when presenting a non-repeated Gaussian noise stimulus (Fig. 1D) (Chichilnisky, 2001) and we quantified response kinetics from these STA waveforms by measuring the time of zero-crossing (between trough and peak) as well as the ratio of amplitudes of the trough and peak (biphasic index). ON-T RGC STAs were significantly more biphasic (biphasic index = 0.63 ± 0.07; mean ± S.D.; n = 15) than those measured for ON-S RGCs (biphasic index = 0.43 ± 0.11; mean ± S.D.; n = 13) (Fig. 1E, right), consistent with their more transient response kinetics that are apparent with step stimuli (Fig. 1B). ON-T RGC responses were also slightly delayed (zero-cross time = - 0.080 ± 0.0063 sec; mean ± S.D.; n = 15) relative to those of ON-S RGCs (zero-cross time = -0.072 ± 0.0052 sec; mean ± S.D.; n = 13) (Fig. 1C, bottom and 1E, left). We used the STA to quantify spiking behavior because it provides a convenient model of RGC temporal response properties. However, it should be noted that the STA alone does not capture all differences between the RGC spike responses – e.g. the discreteness of the ON-T responses in Figure 1C.

Bipolar cell to RGC synapses are an important site of signal diversification in ON pathways

A variety of mechanisms could potentially contribute to the distinct temporal response characteristics of ON-T versus ON-S RGCs, including differences in excitatory and/or inhibitory input conveyed by presynaptic circuits. Parallel visual channels are initially established by the divergence of cone signals to different cone bipolar cell subtypes, which have axons that terminate at distinct depths within the IPL and can correspondingly contact distinct RGC types (Euler et al., 2014; Wässle et al., 2009). We therefore sought to understand to what extent kinetic differences in bipolar cell-mediated excitatory synaptic input could account for transient versus sustained responses in these RGCs.

To do this, we used somatic whole-cell voltage-clamp recordings to measure excitatory synaptic currents from both RGC types while stimulating the retina with the same spatially uniform Gaussian noise stimulus we used when measuring RGC spike output (Fig. 2A). We used these measurements to construct linear-nonlinear (LN) models comprised of a linear temporal filter (Fig. 2B and Fig. S2A) and a time-invariant (static) nonlinearity (Fig. S2B) that provide a simple estimate of the transformation between visual input and excitatory synaptic input to each RGC type (Kim and Rieke, 2001). LN models for each RGC type accurately predicted measured responses to noise stimuli that were not used to construct the models, although LN models of ON-S RGC responses performed better than those for ON-T RGCs (correlation coefficient between average response to repeated noise stimulus and model prediction: 0.61 ± 0.057 (ON-S, n = 9) and 0.50 ± 0.13 (ON-T, n =11), mean ± S.D.; p = 0.028 Wilcoxan rank-sum test). This may in part be because ON-T stimulus-evoked excitatory currents were biased towards large amplitude events compared to those of ON-S RGCs (Fig. 2A, Fig. S1B), similar to the distinct amplitude distributions of spike events in these cell types noted above (Fig. 1C and Fig. S1A). The linear filter captures the kinetics of the RGC response and is analogous to the time-reversed STA derived from spike responses (Chichilnisky, 2001). As with the STAs in Figure 1D, excitatory linear filters were slower and more biphasic in ON-T (zero-cross time = 0.10 ± 0.013 s; biphasic ind. = 0.45 ± 0.090; mean ± S.D.; n = 13) compared to ON-S RGCs (zero-cross time = 0.083 ± 0.0074 s; biphasic ind. = 0.31 ± 0.10; mean ± S.D.; n = 15) (Fig. 2C). This latter difference is consistent with more transient light-evoked excitatory synaptic input to ON-T RGCs. Indeed, light step-evoked excitatory currents to ON-T RGCs decayed rapidly to baseline levels within a few hundred milliseconds, even in the continued presence of light input, whereas excitatory inputs to ON-S RGCs had a sustained component that persisted for the duration of the light step (Fig. 2D-E).

These results show that transient versus sustained kinetics are already present in the excitatory pathways that provide input to ON-T and ON-S RGCs. These findings do not rule out additional contributions to the distinct spiking behavior of these RGC types from amacrine cell-mediated inhibitory synaptic input to the RGCs or from different intrinsic spiking properties. However, the clear differences we observed in excitatory synaptic input between ON-T and ON-S RGCs indicates that bipolar cell pathways have a central role in establishing transient versus sustained kinetics.

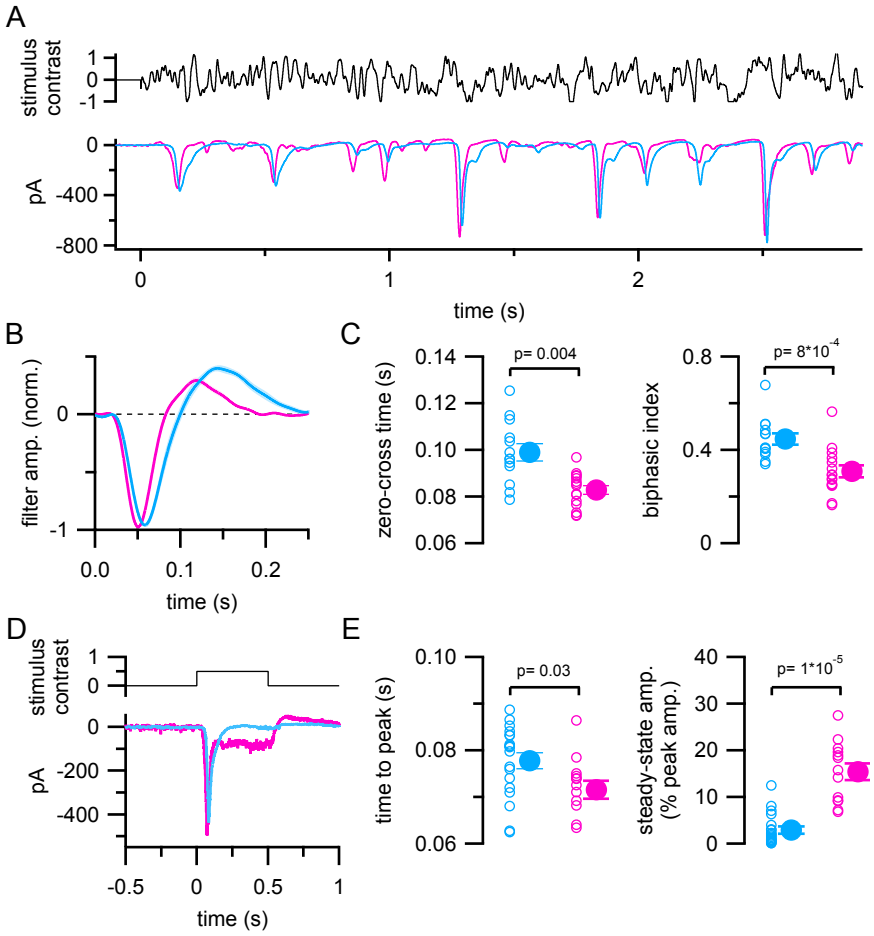

***Figure 2**. Distinct excitatory synaptic input to ON-T and ON-S RGCs. (A) Excitatory synaptic currents measured in example ON-T (cyan) and ON-S (pink) RGCs in response to same Gaussian noise stimulus as in Fig. 1. Traces show average currents from ten repetitions of the same stimulus and are baseline subtracted to facilitate comparison. (B) Linear filters computed from responses to non-repeated noise stimulus presentation. Lines and shaded areas show mean ± SEM of responses from ON-T (n= 13) and ON-S (n= 15) RGCs. (C) Quantification of filter kinetics in different RGCs. (D) Excitatory currents measured from example ON-T and ON-S RGCs in response to a 0.5 second step increase in light intensity (50% contrast; mean response to five repetitions of stimulus). (E) Quantification of step response kinetics (n= 19 ON-T RGCs; n= 13 ON-S RGCs). In (C) and (E) open circles show measurements from individual cells and filled circles with error bars show mean ± SEM values. Significance values from Wilcoxan rank sum tests.*

ON-T and ON-S RGCs receive input from distinct bipolar types

In general, retinal circuits dedicated to transient versus sustained signaling are located at the center and borders of the IPL, respectively (Baden et al., 2016; Bae et al., 2018; Franke et al., 2017; Roska and Werblin, 2001). We compared stratification patterns of ON-T and ON-S RGCs in a subset of whole-cell recordings by filling cells with a fluorescent dye and imaging the dendrites of physiologically-characterized RGCs using two-photon microscopy. We assessed IPL depth in live tissue by using retinas from a transgenic mouse line in which type 5 bipolar cells strongly express EGFP (*Gjd2-EGFP* mice). These EGFP+ bipolar cells have axons that occupy a narrow band just above and overlapping with the dendrites of ON starburst amacrine cells (Fig. S3A) and express calcium binding protein 5 (CaBP5) (Fig. S3B-D) (Ghosh et al., 2004). Based on the regular spacing of their somas, these cells likely correspond to one of the three subtypes of type 5 bipolar cells previously identified in mouse retina (Greene et al., 2016; Rodieck, 1991) (Fig. S3E-F). Imaging of RGCs together with EGFP+ axon terminals in *Gjd2-EGFP* mice revealed that ON-T and ON-S RGC dendrites occupy distinct, mostly non-overlapping regions of the IPL (Fig. S4).

The distinct IPL stratification of ON-T and ON-S RGCs indicates they receive input from different bipolar cell populations. A recent connectomic analysis that used a published electron microscopy data set from mouse retina (Ding et al., 2016) found that type 6 and type 7 bipolar cells account for ~50% and 46% of the excitatory synapses formed upon ON-S RGC dendrites, respectively (Sabbah et al., 2018). However, the bipolar cell subtype(s) presynaptic to ON-T RGCs have not previously been identified. Our observation that ON-T RGC dendrites occupy a narrow band in the IPL that very closely matches the stratification pattern of EGFP+ type 5 bipolar cell axons in *Gjd2-EGFP* mice (Fig. S5) suggests that these bipolar cells likely provide a substantial fraction of the excitatory input to ON-T RGCs. To test this possibility, we transfected retinas from *Gjd2-EGFP* mice with a plasmid encoding PSD-95 fused to the red fluorescent reporter mCherry to label postsynaptic sites of excitatory input (Fig. S5). We quantified the fraction of putative synapses, defined as sites with overlapping PSD-95 and EGFP fluorescent signals, that arose from *Gjd2-EGFP*+ axon terminals using confocal microscopy (Schwartz et al., 2012). From this analysis, we concluded that the labeled type 5 bipolar cells in *Gjd2-EGFP* mice provide ~40% of the ribbon synaptic input to ON-T RGCs (Fig. S5D).

We next performed correlative fluorescence imaging and serial block-face scanning electron microscopy (SBFSEM) to identify which type 5 bipolar subtype is labeled in Gjd2-EGFP mice and to further characterize what other bipolar cell types provide the remaining input to ON-T RGCs. We first used 2P microscopy to image the dendritic morphology of two dye-filled ON-T RGCs that were identified from their light-evoked spike responses in flat-mounted retina from *Gjd2-EGFP* transgenic mice (Fig. 3A). After 2P imaging, we fixed the retina and used the near infrared branding (NIRB) technique to create fiducial marks in the tissue around the dye-filled ON-T RGCs (Bishop et al., 2011). After acquiring the SBFSEM volume, we located the somas of the two ON-T RGCs using these fiducial marks and reconstructed the dendritic arbors of both cells (e.g. Fig. 3B). The dendritic morphologies from our EM reconstruction matched those from the light microscopy images. This suggests that we successfully identified the two ON-T RGCs recorded physiologically in our EM volume. We chose the two longest dendritic arbors from the RGC soma to the dendritic tip and identified all the synapses from bipolar cells along these dendrites (Fig. 3C). We then reconstructed all the presynaptic bipolar cells and classified them according to their axon morphology and stratification (Fig. 3D). Careful examination of axonal tiling among type 5i, 5o and 5t subtypes provided additional confirmation of the classification of these type 5 bipolar cells (Fig. S6A) (Greene et al., 2016). When comparing the EM images with light microscopy images, it is clear that *GJD2-GFP*+ bipolar cells are type 5i bipolar cells (Fig. S6B).

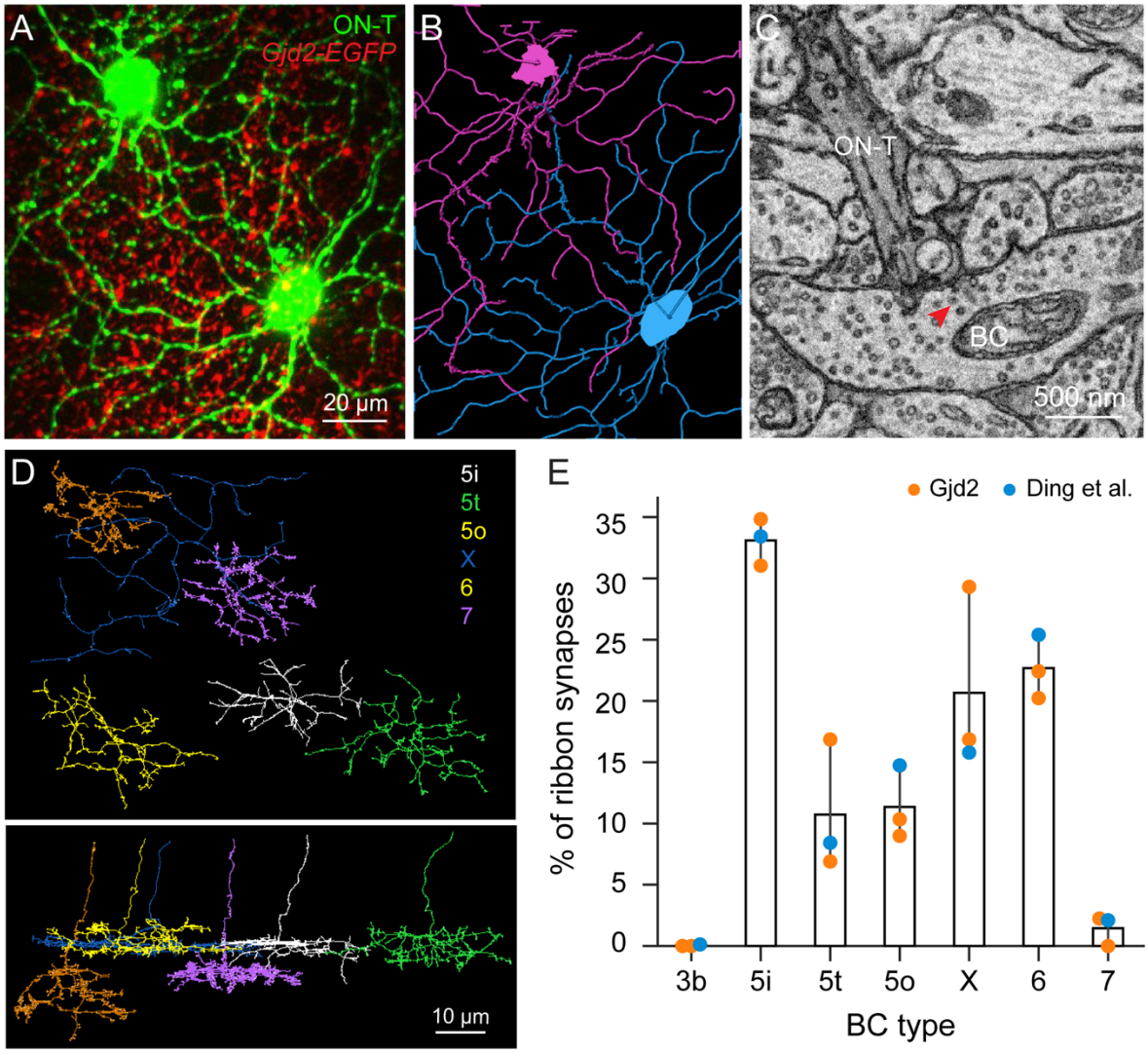

***Figure 3**. Identification of bipolar cell subtypes presynaptic to ON-T RGCs. (A) Maximum-projections z-stacks of two dye-filled ON-T RGCs (green) in wholemount retina from Gjd2-EGFP (red) transgenic mice. (B) Traced skeletons of dendritic arbors of the two ON-T RGCs from EM volume. (C) An EM micrograph showing a ribbon synapse (arrowhead) on a BC axonal terminal onto the dendrite of a ON-T RGC. (D) An example skeleton for each presynaptic BC type (types 5i, 5t, 5o, X, 6 and 7) of ON-T RGCs. Top: whole-mount view, Bottom: side view. (E) Bar plot showing the proportion of input synapses to ON-T RGCs from each BC type. Mean ± SEM (n=3 RGCs, 2 from this study and one from Ding et al. (2016)).*

Results from the SBFSEM reconstructions agreed closely with those from the light microscopy approach described above. Type 5i bipolar cell axon terminals provided the largest fraction of synapses onto the two ON-T RGCs within our SBFSEM volume (~30-35%). Other inputs arose from type 5o (~10%), type 5t (~5-15%), XBC (~15-30%), and, somewhat surprisingly given the differences in stratification, from type 6 (~20%) bipolar cells (Fig. 3E). We confirmed this connectivity pattern by additionally analyzing bipolar cell synaptic inputs to a putative ON-T RGC

(RGC7089) in the same publicly available SBFSEM volume (Ding et al., 2016) that was used by Sabbah et al., (2018) to map inputs to ON-S RGCs (Fig. 3E).

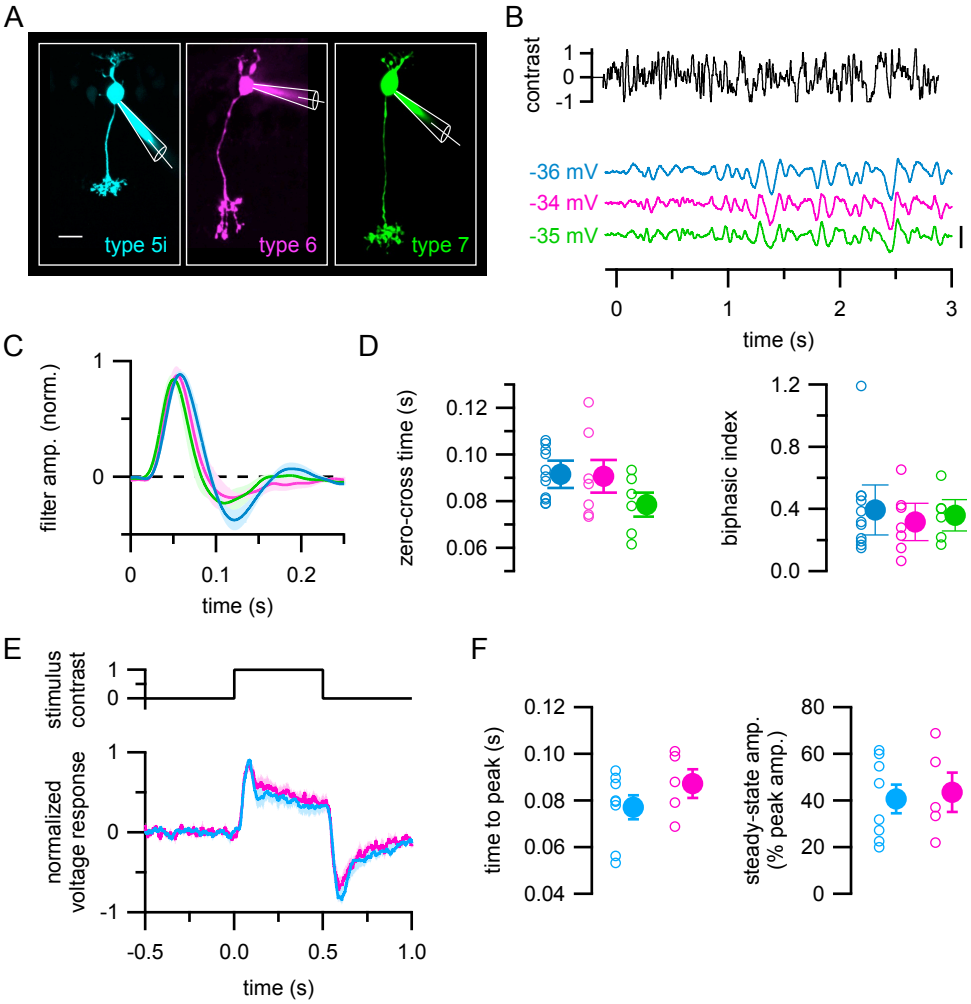

Figure 4*. Bipolar cell subtypes presynaptic to ON-T and ON-S RGCs have indistinguishable temporal response properties. (A) Maximum-projection z-stacks of fluorescent dye-filled bipolar cells targeted for electrophysiological recording in retinal slices from Gjd2-EGFP (left), Grm6-tdTomato (middle), and Gus8.4-EGFP (right) transgenic mice. (B) Responses to spatially uniform Gaussian noise stimulation (same as in Figs. 1-2) in example type 5i (cyan), type 6 (magenta) and type 7 (green) bipolar cells. Voltage traces are average responses to ten repetitions of the noise stimulus. (C) Linear filters computed from responses to non-repeated noise stimulus presentation. Lines and shaded areas show mean ± SEM of responses (type 5i, n= 11; type 6, n= 7; type 7, n= 6). (D) Quantification of response kinetics from linear filters. No significant differences across types (p = 0.19 zero-cross times; p= 0.89 biphasic index; Kruskal-Wallis test). (E) Responses to step light increment. Lines and shaded areas show peak-normalized mean ± SEM responses across type 5i bipolar cells (n= 8) and type 6 bipolar cells (n= 5). (F) Quantification of step response kinetics. Time to peak and steady-state response amplitude were not different between type 5i and type 6 bipolar cells (p= 0.72 and p= 0.35, respectively; Wilcoxan rank sum test).*

Bipolar cell light responses differ minimally across types

Are transient versus sustained excitatory inputs inherited from the response properties of the different bipolar cells presynaptic to ON-T and ON-S RGCs? Or is the distinct excitatory synaptic input these RGCs receive primarily due to differences at the bipolar cell to RGC synapse? To answer these questions, we compared the light-driven response properties of the bipolar cell subtypes that comprise most of the excitatory input to ON-T or ON-S RGCs. We made targeted electrophysiological recordings from type 5i, type 6 and type 7 bipolar cells in retinal slices from three transgenic mouse lines in which these different bipolar cell subtypes express fluorescent proteins (see Methods). In these experiments, we used somatic whole-cell perforated-patch recordings to limit perturbation of the G-protein signaling cascade that mediates ON bipolar cell light responses.

Somatic resting membrane potentials did not differ significantly among these bipolar cell types (mean ± S.D. V_{rest}: -38 ± 6.3 mV in type 5i (n= 11); -33.7 ± 6.3 mV in type 6 (n= 7); - 36.5 ± 4.7 mV in type 7 (n=6); Kruskal-Wallis test, p= 0.35). We characterized light responses using the same spatially uniform Gaussian noise stimulus (Fig. 4B) and linear-nonlinear model analysis (Fig. 4C and Fig. S7) as in RGC recordings to facilitate direct comparison of results from bipolar cells and RGCs (Kim and Rieke, 2001; Rieke, 2001). LN models of bipolar cell responses accurately predicted responses to noise stimuli (correlation coefficient between average response to repeated noise stimulus and LN model prediction = 0.75 ± 0.15 for n = 18 bipolar cells (n = 13 type 5; n = 3 type 6; n = 2 type 7)). Unlike for ON-T and ON-S RGCs, temporal characteristics of type 5i, type 6 and type 7 bipolar cell linear filters were indistinguishable from each other under our recording conditions (Fig 4B-D). Although there was some variability in the temporal response properties across the population of bipolar cells we recorded, these differences were not associated with morphologically and molecularly defined bipolar cell types. Rather, we observed variability in response kinetics within each bipolar cell subtype and temporal responses thus overlapped substantially across different type 5i, type 6 and type 7 bipolar cells (Fig. 4 and Fig. S7).

Responses to light steps measured in a subset of type 5i and type 6 bipolar cell recordings confirmed our conclusion from Gaussian noise stimuli that different bipolar cell types exhibit nearly identical light response kinetics under our recording conditions (Fig. 4E-F). Unlike the clear differences in light step-evoked excitatory currents we measured in ON-T and ON-S RGCs (Fig. 2D-E), type 5i and type 6 bipolar cells both had sustained responses to light steps. These findings indicate that mechanisms upstream of the generation of the cone bipolar cell voltage response, such as synaptic transmission from cones to cone bipolar cells and intrinsic response properties of the cone bipolar cells, cannot explain the kinetically distinct responses in parallel ON channels mediated by type 5i, type 6 or type 7 bipolar cells.

Presynaptic inhibition does not establish kinetic differences in bipolar cell-mediated excitation

Bipolar cells participate in diverse inhibitory circuits with amacrine cells, which are comprised of >40 morphologically and functionally distinct cell types (Diamond, 2017; Helmstaedter et al., 2013). Recent work suggests that amacrine cell-mediated presynaptic inhibition is critical to bipolar cell subtype-specific patterns of light-evoked glutamate release (Franke et al., 2017). Our bipolar cell voltage recordings, which should reflect a combination of light-evoked excitatory and inhibitory input, argue against the involvement of presynaptic inhibition in generating differential bipolar cell synaptic output between type 5i, type 6 and type 7 bipolar cells. However, the slicing procedure we used to prepare tissue for bipolar cell recordings may damage some inhibitory connections, especially long-range amacrine cell inputs. Distance-dependent

attenuation of voltage signals between bipolar cell axon terminals and the somatic recording site could also limit our ability to accurately measure the influence of presynaptic inhibition in these recordings. We therefore performed additional anatomical and pharmacological experiments to investigate a possible role for presynaptic inhibition in generating kinetically distinct excitation to ON-T and ON-S RGCs.

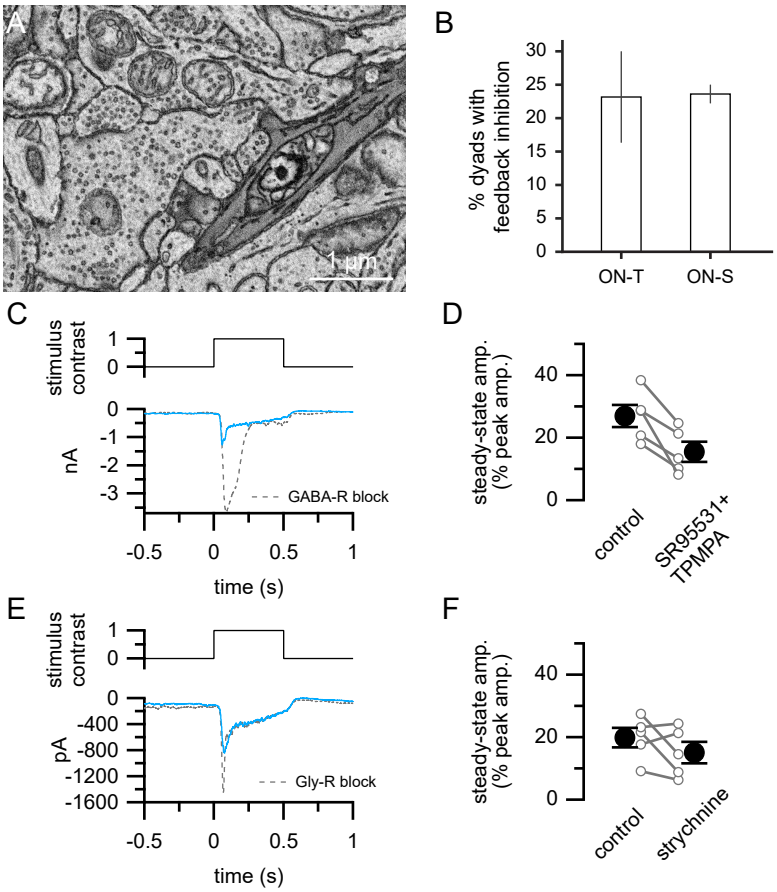

***Figure 5**. Presynaptic inhibition does not establish kinetic differences between bipolar cell inputs to ON-T versus ON-S RGCs. (A) Example EM micrograph showing a ribbon dyad (red arrowhead) between a BC and an ON-T RGC and an amacrine cell, with an adjacent feedback inhibitory synapse (yellow asterisk). (B) Bar plots showing the percentage of RGC/AC ribbon dyads with feedback inhibition. Mean ± SEM (n=2 ON-S RGCs, 2 ON-T RGCs) (C) Excitatory currents measured in response to light step increment in control conditions (cyan) and in the presence of GABA receptor antagonists (10 µM SR95531 and 50 µM TPMPA; dashed gray) in an example ON-T RGC. Traces are mean response from six repeats of stimulus presentation. (D) Summary of steady-state amplitudes measured from step responses in control or with GABA receptor antagonists. No significant difference between conditions (p= 0.063; Wilcoxan signed rank test) (E) Control excitatory currents (cyan) or with addition of strychnine (1 µM; dashed gray) to bath in an example ON-T RGC. (F) Summary of strychnine experiments. No significant difference between conditions (p= 0.438; Wilcoxan signed rank test). In (D) and (F), open circles with lines show measurements from individual ON-T RGCs. Filled circles with error bars show mean ± SEM.*

Many bipolar cell output synapses are organized into a “dyad” arrangement in which a bipolar cell ribbon synapse releases glutamate onto the processes of two different postsynaptic cells. At dyads, bipolar cell output synapses can be presynaptic to the processes of two amacrine cells, two RGCs, or an amacrine cell and a RGC (Cohen and Sterling, 1990; Dowling and Boycott, 1966; McGuire et al., 1984; Yu et al., 2023). Dyad synapses comprised of an amacrine cell and a RGC may shape bipolar cell glutamate release dynamics onto the RGC partner because glutamatergic excitation of the postsynaptic amacrine cell can elicit release of inhibitory neurotransmitters (GABA or glycine) from the amacrine cell processes that feed back onto the bipolar cell axon terminal. This form of inhibitory feedback control of bipolar cell output, termed reciprocal inhibition, could potentially contribute to differences in glutamate release onto ON-T and ON-S RGCs.

We analyzed bipolar cell dyads with postsynaptic amacrine cell processes and either ON-T or ON-S RGC dendrites in SBFSEM volumes to examine whether reciprocal inhibition is likely to generate more transient glutamate release onto ON-T RGCs. We defined putative reciprocal synapses as bipolar cell/amacrine cell/RGC dyads in which we observed clustered vesicles within the amacrine cell process that were within close proximity of the bipolar cell ribbon synapse (Fig. 5A). Our ultrastructural analysis revealed that the prevalence of reciprocal synapses was similar at dyad synapses with postsynaptic ON-T versus ON-S RGCs (Fig. 5A-B). This finding is not consistent with an important role for feedback/reciprocal inhibition in generating differential bipolar cell output onto the different RGC types.

We also performed pharmacological experiments to further examine what role, if any, inhibition may have in establishing transient glutamate release onto ON-T RGC dendrites. We used ACSF in place of Ames solution for the dissection and maintenance of tissue for these experiments. ACSF is often used in retina experiments, including the glutamate release measurements describe below, and we wanted to check that our results generalized across conditions. Light step-evoked currents in both ON-T and ON-S RGCs were more sustained than responses measured using Ames’ solution (Fig. S8A-B). Nonetheless, the relative differences between RGC types appear to be maintained across different experimental conditions.

Blockade of $GABA_A$ and $GABA_C$ receptors via bath co-application of SR95531 and TPMPA enhanced both the initial transient component and the sustained component of light step-evoked excitatory synaptic currents in ON-T RGCs (Fig. 5C). The strong enhancement of the initial phase of the response we observed is consistent with prior work showing that $GABA_C$ receptor-mediated inhibition limits multivesicular release from bipolar cells (Sagdullaev et al., 2006). On average, block of GABA receptors did not significantly change in the ratio of sustained versus transient components of excitatory inputs to ON-T RGCs compared to control conditions (Fig 5D). If anything, these drugs tended to make excitatory currents more transient, which is the opposite effect expected if presynaptic GABA receptors contribute to generating transient responses in these cells. Thus, GABAergic inhibition appears to control response gain but not kinetics of bipolar cell synaptic output to ON-T RGCs. Similarly, we found that glycinergic inhibition is not likely to contribute importantly to more transient glutamate release from bipolar cells presynaptic to ON-T RGCs; bath application of the glycine receptor antagonist strychnine did not significantly alter the kinetics of light step-evoked excitatory currents in these cells (Fig. 5E-F). Taken together with our ultrastructural analysis, these results show that amacrine cell-mediated inhibition of bipolar cell axon terminals does not contribute to kinetic differences in excitatory synaptic input to ON-T and ON-S RGCs.

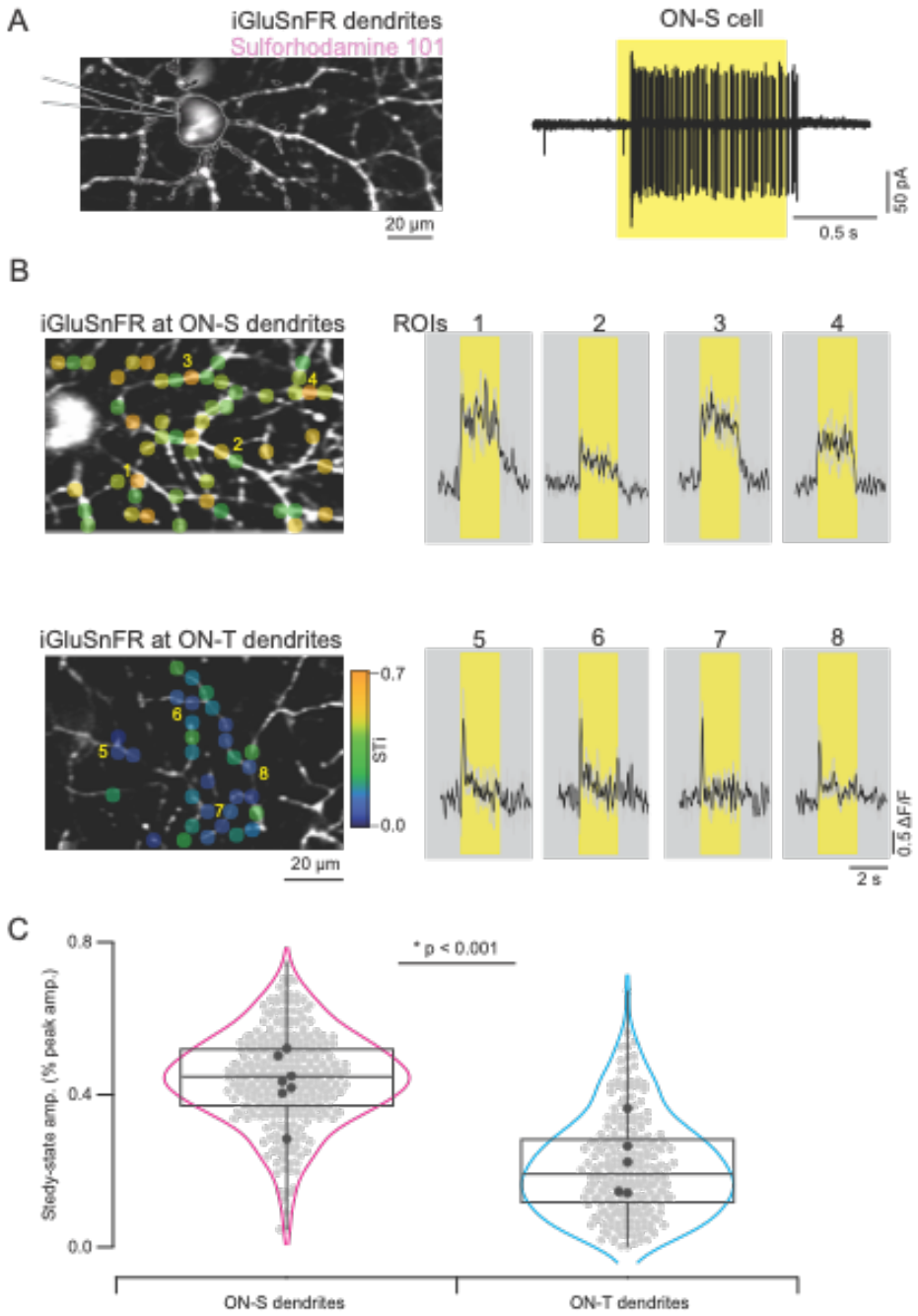

***Figure 6**. Distinct glutamate input kinetics at ON-S vs ON-T RGC dendrites. (A) ON-S RGC dendrites expressing iGluSnFR in a KCNG-Cre mouse were filled with sulforhodamine 101 (left) after measuring their spiking response to a 200 µm spot extracellularly (Right). Yellow bands indicate stimulus duration. (B) iGluSnFR expressing ON-S and ON-T dendrites at different depths of the inner-plexiform layer (Left) were imaged using two-photon microscopy. Example iGluSnFR signals extracted from small regions of interest (ROIs 1-8) from ON-S and ON-T RGC dendrites illustrate the kinetic differences in their respective inputs. Black, mean responses; gray, individual trials. (C) Distribution of steady-state response amplitudes of the individual (gray) and average (black) ROIs from different recordings done from ON-S and ON-T dendritic field of views evoked by a 200 µm static spot (n = 7 FOVs, 6 retinas for ON-S and 5 FOVs, 5 retinas for ON-T RGC dendrites, *p<0.001; t-test).*

Bipolar cell glutamate release differs across types

Taken together, the bipolar cell and RGC recordings in Figures 2 and 4 indicate that bipolar cell synapses have a key role in the separation of visual signals into transient or sustained channels within ON pathways in the retina. Presynaptic and/or postsynaptic mechanisms could contribute to the distinct kinetics of bipolar cell-mediated excitatory input to ON-T and ON-S RGCs. To investigate whether presynaptic differences in glutamate release from bipolar cell axon terminals shape RGC response kinetics, we expressed the fluorescent glutamate reporter iGluSnFR on the dendrites of ON-T and ON-S RGCs. Using two-photon glutamate sensor imaging, we found that light-evoked glutamate signals had significantly faster kinetics at ON-T RGC dendrites (steady-state amplitude as % of peak amplitude = 21 ± 13; mean ± S.D.; n = 224 ROIs) compared to those associated with ON-S RGC dendrites (steady-state amp. (% of peak amp.) = 44 ± 12; mean ± S.D.; n = 307 ROIs) (Fig. 6). These results show that differences in glutamate release from presynaptic bipolar cells contribute to transient versus sustained ON RGC responses. However, these experiments do not rule out the possibility that additional postsynaptic mechanisms, for example differential glutamate receptor expression, may also contribute to kinetic differences between RGC types.

Although whole-cell excitatory currents in ON-T and ON-S RGCs (Fig. 2, Fig. S8) and iGluSnFR signals measured from ON-T and ON-S RGC dendrites (Fig. 6) both exhibited clear kinetic differences between the RGC types, there were quantitative differences in the response to light steps between the different measurement approaches. As described above, these differences appear to arise from differences in the external solution (Ames vs ACSF). The iGluSnFR experiments used an ACSF solution, like the patch-clamp experiments in Figs. 5 and S8. Both iGluSnFR responses and excitatory synaptic inputs measured in ACSF showed a larger sustained component of the step response at both ON-T and ON-S dendrites compared to currents measured in Ames (compare Fig. 2D-E, Fig. S8A-B and Fig. 6B-C). This observation highlights the importance of comparing responses between different RGC types, as well as between RGCs and bipolar cells, under identical recording conditions.

Importantly, the kinetics of glutamate release measured using iGluSnFR are much more similar to the excitatory synaptic inputs to ON-T and ON-S RGCs than they are to the relevant bipolar voltage responses (Fig 4). This indicates that the difference between the ON-T and ON-S responses originates at least in part in the conversion of bipolar voltage to glutamate release.

Ribbon size and vesicle replenishment

Prior work has shown that bipolar cells can exhibit profound short-term depression of glutamate release due to use-dependent depletion of the readily-releasable pool of synaptic vesicles (Burrone and Lagnado, 2000; Singer and Diamond, 2006, 2003; von Gersdorff and Matthews, 1997). Strong vesicle depletion at the cone bipolar cell synapses onto ON-T RGCs could generate more transient responses in these cells compared to ON-S RGCs. To examine this possibility, we used a paired flash stimulus paradigm, in which two brief light flashes separated by varying time intervals were presented while measuring excitatory synaptic currents in ON-T or ON-S RGCs. As in Figures 1, 2 and 4, we used Ames' medium for tissue preparation and maintenance in these experiments.

Flash-evoked excitatory synaptic currents were suppressed in both RGC types at short inter-flash intervals, consistent with incomplete recovery from vesicle depletion at the time of the second flash (Fig. 7A top/middle, B). However, the extent of suppression was much stronger for currents measured in ON-T RGCs compared to ON-S RGCs. We quantified the extent of

suppression using a paired flash ratio, which was calculated as the peak amplitude of the response to the second flash divided by the peak amplitude of the response to the first flash. At the shortest interval we tested (50 ms), the response to a second flash was almost completely suppressed in ON-T RGCs (paired flash ratio = 0.04 ± 0.01; mean ± SEM) whereas the response to a second flash in ON-S was suppressed considerably less (paired flash ratio = 0.29 ± 0.04). To rule out the possibility that a reduction in bipolar cell voltage response to the second flash could account for the strong paired flash suppression of excitatory input to RGCs, we also measured type 5i bipolar cell responses to the paired flash stimuli. The amplitude of flash-evoked voltage responses in type 5i bipolar cells was unchanged by a preceding flash at all time intervals (Fig. 7A bottom, C), which argues that paired flash suppression arises at the bipolar cell synaptic terminal. These results are consistent with the idea that differences in the extent of stimulus-evoked vesicle pool depletion in bipolar cells could underlie transient versus sustained excitatory input to ON-T and ON-S RGCs.

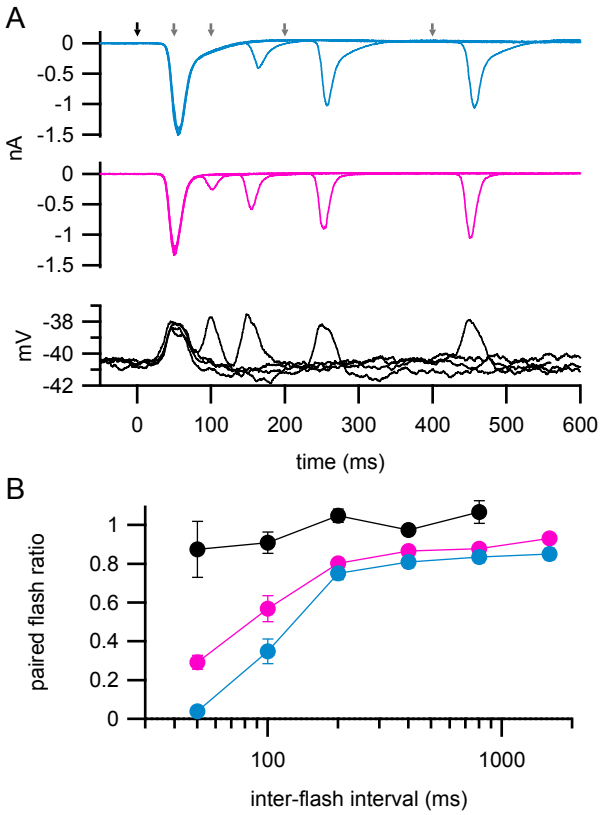

Figure 7. *Stronger flash-evoked suppression of excitatory currents in ON-T versus ON-S RGCs. (A) Paired flash-evoked excitatory currents measured at different inter-flash intervals (50, 100, 200, 400 ms) in an example ON-T (top; cyan) and an ON-S (middle, magenta) RGC. Bottom black traces show voltage responses to same stimulus measured in an example type 5i bipolar cell. Arrows at top indicate timing of first flash (black) and second flashes (gray). Flashes were 400% contrast and 10 ms duration. Traces show mean responses to five repeats of each paired flash interval. (B) Filled circles with error bars show mean ± SEM paired-flash ratios at different inter-flash intervals across all ON-T RGCs (cyan; n= 6), ON-S RGCs (magenta; n= 5) and type 5i bipolar cells (black; n= 6).*

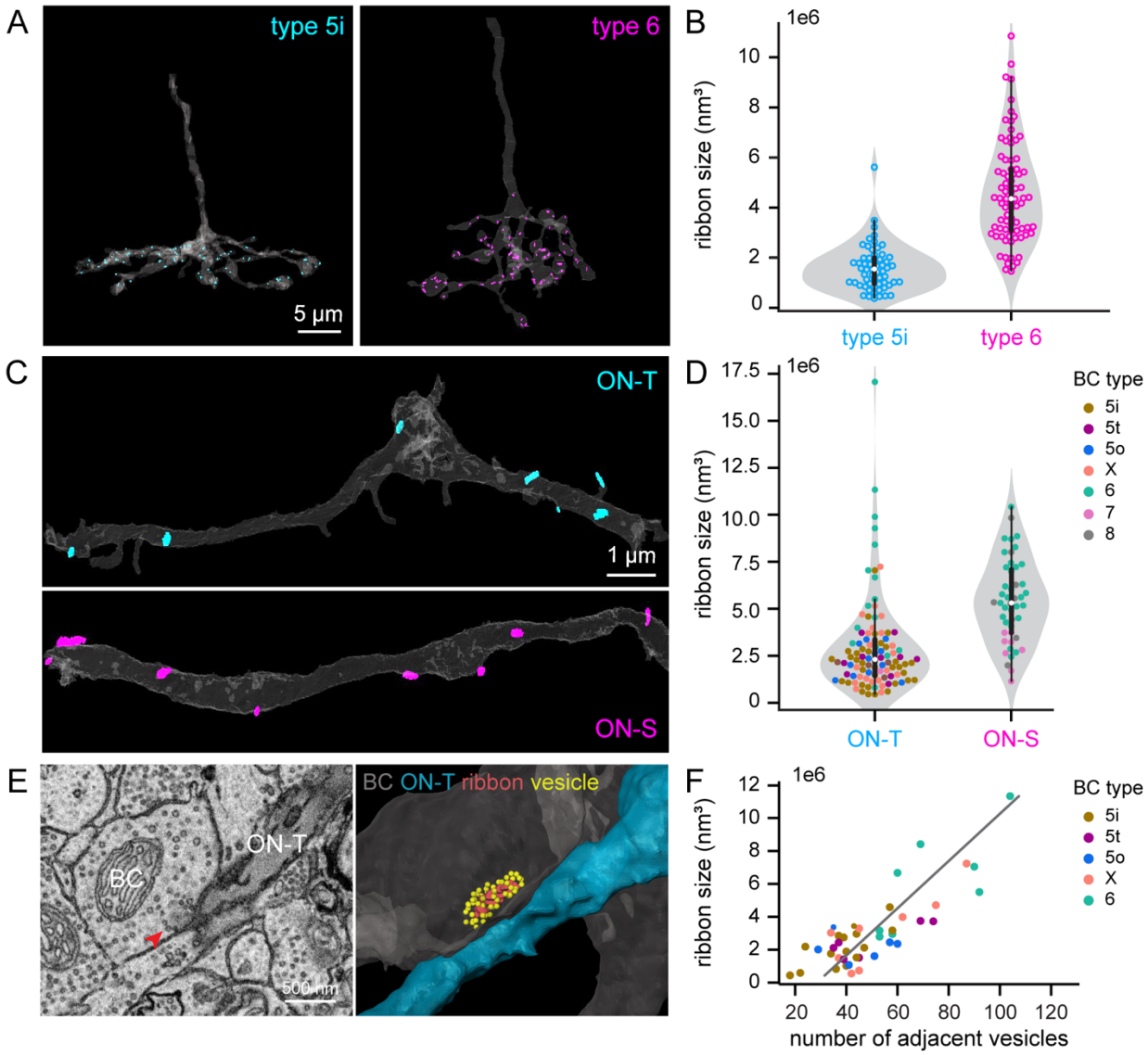

Figure 8. *Bipolar cell subtype-specific differences in ribbon size. (A) 3D reconstructions showing segmented axon stalk and axonal terminal (gray) and all the synaptic ribbons within the axonal terminal a type 5i (cyan) and a type 6 (magenta) BC. (B) Violin plot showing distribution of ribbon volumes (each data point is a ribbon) for the type 5i and type 6 BC in (A). The boxes indicate the interquartile range (thick lines, 25%-75%), median value (white dot), and 1.5 times interquartile range (thin line). Shaded gray areas represent rotated kernel density plots. (C) 3D reconstructions showing segmented dendritic arbor (gray) and all the synaptic ribbons presynaptic to these segments of ON-T (cyan) or ON-S (magenta) RGC dendrites. (D) Violin plot with scattered dots showing ribbon volumes for each ribbon presynaptic to a stretch of reconstructed ON-T or ON-S RGC dendrite. Each ribbon (dot) is colored differently for each BC type. (E) An EM micrograph (left) and 3D reconstruction (right) of a ribbon and its adjacent vesicles. The ribbon is indicated by the red arrow in the EM image. In the 3D reconstruction, yellow dots indicate the adjacent vesicles surrounding the presynaptic ribbon (red) in the BC terminals (gray). Postsynaptic ON-T RGC is in blue. (F) Scatter plot showing ribbon size in volume in relationship with the number of adjacent vesicles. Gray line represents the linear regression model fitted to the data. Linear regression:* $\beta = 6.98e{-}06$, $p < 0.001$, $r^2 = 0.66$.

We next looked for ultrastructural correlates of differential synapse function in bipolar cell axon terminals reconstructed from SBFSEM volumes. Interestingly, type 6 bipolar cell synaptic ribbons were ~2-3 fold larger than those of types 5i bipolar cells (Fig. 8A-B). These differences did not depend on the identity of the postsynaptic RGC partner (Fig. 8D). Ribbons in XBCs, type 5o and type 5t bipolar cells were also smaller than type 6 bipolar cell ribbons (Fig. 8D). This bipolar cell subtype-specific difference in ribbon size and the difference in ratio of type 6 to type 5i input between RGC types meant that ribbons were on average smaller at synapses made on ON-T compared to ON-S dendrites (Fig. 8C-D).

We found that ribbon size of several ON bipolar cell types is strongly correlated with the total number of vesicles that are in close contact with the synaptic ribbon across different bipolar cell types (Fig. 8E-F). Ribbon-associated vesicles are thought to correspond to the releasable pool of vesicles, comprised of both a readily-releasable pool that are docked at the presynaptic active zone as well as a reserve pool of vesicles that are bound to the ribbon at more distal sites (Lagnado and Schmitz, 2015). These two vesicle pools exhibit distinct release kinetics, with the readily-releasable pool corresponding to the fastest phase of glutamate release and the reserve pool contributing to slower glutamate release that occurs with prolonged stimuli (Mennerick and Matthews, 1996; Neves and Lagnado, 1999). Our observations that the average excitatory synaptic input to ON-T RGCs is smaller and that most excitatory input to ON-T cells originates from bipolar synapses with fewer ribbon-associated vesicles are consistent with a role for vesicle depletion in establishing transient glutamate release onto these RGCs. The larger pool of ribbon-associated vesicles in type 6 bipolar cell terminals, which comprise ~ 55% of the synaptic input to ON-S RGCs, may support sustained synaptic transmission onto these RGCs.

Discussion

In this study, we sought to understand how kinetically distinct visual pathways are established in the retina by directly comparing the visual response properties of transient and sustained ON RGCs with their presynaptic bipolar cells. Our results show that bipolar cell synapses have a key role in establishing different temporal channels in ON circuits of the retina. Further, amacrine cell-mediated presynaptic inhibition does not appear to account for transient versus sustained bipolar cell synaptic output. Rather, bipolar cell subtype-specific differences in synaptic release properties likely generate kinetically distinct output to postsynaptic targets. Our anatomical analysis suggests that these differences may at least in part be due to differences in synaptic vesicle pool size.

A key aspect of our work is that we measured RGC and bipolar cell responses using identical stimuli and under the same experimental recording conditions. To our knowledge, a direct comparison of RGC responses with those of their presynaptic bipolar cells has not previously been reported. The importance of measuring RGC and bipolar cell responses under the same conditions is highlighted by our observation that excitatory synaptic currents measured in ON alpha RGCs exhibited quantitatively different kinetics, although relative differences between types were preserved, when measurements were made from retinas maintained in ACSF versus Ames' bath solution (compare Fig. 2 (Ames') and Figs. 6 and S8 (ACSF)).

We found that the bipolar cell subtypes that provide the major input to ON-T (type 5i) or ON-S RGCs (types 6 and 7) had indistinguishable light-evoked voltage responses (Figure 4). This was not entirely surprising given that most or all ON cone bipolar cell subtypes are indirectly coupled to other nearby ON cone bipolar cells via electrical synapses between bipolar cell axon terminals and the distal processes of AII amacrine cells. These electrical synapses form the basis for the primary rod pathway that mediates vision under dim light conditions, but lateral

signals can also flow among neighboring bipolar cells under conditions where cone signaling dominates (Demb and Singer, 2012). Indeed, a substantial fraction (~30-50%) of light-evoked responses in the bipolar cell types we investigated here can be attributed to lateral signals that arrive via electrical synapses at photopic light levels (Kuo et al., 2016). Each AII amacrine cell is electrically coupled to multiple ON cone bipolar subtypes as well as to other AII amacrine cells (Marc et al., 2014; Tsukamoto and Omi, 2017; Veruki and Hartveit, 2002a, 2002b). Different ON cone bipolar cell subtypes may also be directly coupled via gap junctions to each other (Sigulinsky et al., 2020; Tsukamoto and Omi, 2017).

Direct or indirect (via AII) coupling may limit the extent to which different bipolar cells can generate subtype-specific voltage responses. However, our findings differ from a previous study that found some differences among mouse ON cone bipolar cell subtypes. Ichinose et al., (2014) reported that a subset of type 5 bipolar cells, which the authors termed type 5f, and type 7 bipolar cells had more transient responses than type 6 bipolar cells. Methodological differences may account for the discrepancy between our results and the previous work by Ichinose et al., (2014). For example, the previous study measured bipolar cell responses using whole-cell recordings and included inhibitory receptor antagonists in their experimental solutions whereas we used gramicidin perforated-patch recordings and left inhibitory signaling intact. Regardless of the reasons for the different findings, our observation that bipolar cell subtypes exhibited similar responses under the same experimental conditions for which we observed obvious differences among postsynaptic RGCs argues that mechanisms upstream of bipolar cell glutamate release (e.g. cone to bipolar cell synapses or intrinsic voltage response properties of bipolar cells) are unlikely to have a major role in shaping RGC type-specific responses for the stimuli we used here.

A limitation of our work is that we did not record from every one of the bipolar cell subtypes that are presynaptic to ON-T RGCs. Instead, we measured responses from type 5i and type 6 bipolar cells, which together comprise >~50% of the synaptic input to ON-T RGC dendrites. It is possible that the other presynaptic bipolar cell types (type 5o, type 5t and XBC) may have more transient light-evoked voltage responses that could contribute to the transient excitation measured in ON-T RGCs. In fact, a previous study in mouse retina found that XBCs and a subset of type 5 bipolar cells express voltage-gated Na^+ channels (Hellmer et al., 2016). These channels may enhance response transience or might even contribute to the generation of light-driven all-or-none spiking responses in these bipolar cells (Ichinose et al., 2014; Puthussery et al., 2013; Saszik and DeVries, 2012). Despite the possibility that intrinsic response properties of the bipolar cell types we did not record from could contribute to the generation of transient responses in ON-T RGCS, we consider it unlikely that this alone could not account for the kinetics of the excitatory synaptic currents we measured in these RGCs. Type 5i and type 6 bipolar cells have a significant sustained component of their light step-evoked voltage response (Fig. 4E-F), whereas excitatory currents measured for the same stimulus and under the same conditions in ON-T RGCs had little to no sustained component (Fig. 2D-E). Even if the synapses formed by type 5o, type 5t and XBC provide a major fraction of the functional synaptic input to ON-T RGCs (despite our anatomical estimate that together they comprise <50% of the total ribbon input), we would still expect to observe some sustained excitatory input if type 5i and type 6 bipolar cell synaptic output follows the voltage response of these cells. Thus, a marked transformation of the sustained bipolar cell membrane voltage response to a transient synaptic current must take place. Our measurements of extracellular glutamate at ON-T and ON-S dendrites (Fig. 5) suggest much of this transformation occurs at the level of bipolar cell glutamate release. It is interesting to note in this context that ON-T and ON-S RGCs both receive input from type 6 bipolar cells (comprising ~20% and ~50% of total synaptic input, respectively). Due to differences in dendrite stratification, type 6 bipolar cell synapses onto ON-

633 T RGCs arise from a region of the axon that is located more proximal to the bipolar cell soma
634 than the synapses formed onto ON-S RGCs, which are found within the distal axon lobules.
635 However, we did not observe any differences in ribbon size at distal versus proximal locations in
636 type 6 bipolar cell axons (not shown). Whether postsynaptic target-specific synapse function, as
637 has previously been reported in salamander retina (Asari and Meister, 2014, 2012), contributes
638 to signal diversification in circuits involving type 6 bipolar cells will require further investigation.
639
640 Our results indicate that amacrine cell-mediated inhibition at bipolar cell synaptic terminals is not
641 necessary for generating transient glutamate release kinetics onto ON-T RGC dendrites. This is
642 seemingly at odds with prior work that has noted an essential role for surround inhibition in
643 establishing type-specific bipolar cell glutamate release dynamics (Franke et al., 2017).
644 However, we note that our analysis here focused only on whether presynaptic inhibition shapes
645 the kinetics of excitatory inputs to ON-T RGCs. Our anatomical and pharmacological
646 experiments together argue that presynaptic inhibition is not an important factor in the
647 transformation from sustained bipolar cell voltage responses to transient excitatory synaptic
648 currents in ON-T RGCs. This is not to say that amacrine cell-mediated inhibition does not have
649 a role in generating subtype-specific response properties for other aspects of bipolar cell
650 function. Indeed, inhibition does have in important role in establishing differential spatial tuning
651 of excitatory inputs to the RGC types we studied; excitatory synaptic currents in ON-T RGCs
652 exhibit stronger surround inhibition than ON-S RGCs, and this surround inhibition is reduced by
653 bath application of GABA receptor antagonists (Fig. S8C).
654
655 We conclude that transient versus sustained excitatory inputs to ON-T and ON-S RGCs most
656 likely arise from bipolar cell subtype-specific differences in synaptic release properties.
657 Excitatory inputs to ON-T RGCs exhibited stronger paired flash depression than those to ON-S
658 RGCs (Fig. 7), which indicates distinct vesicle cycling dynamics at the bipolar cell axon
659 terminals presynaptic to the different RGC types. Our ultrastructural analysis suggests that
660 bipolar subtype-dependent differences in ribbon-associated vesicle pool size could be a factor in
661 establishing transient versus sustained glutamate release kinetics (Fig. 8). This finding is
662 consistent with the idea that sustained transmission from ribbon synapses is determined by the
663 rate of replenishment of the readily-releasable pool of synaptic vesicles following exocytosis
664 (Lagnado and Schmitz, 2015). It is important to note, however, that type 7 bipolar cells (~45% of
665 excitatory input to ON-S RGCs) have small synaptic ribbons, yet iGluSnFR imaging of type 7
666 bipolar cell axon terminals found that these cells exhibit sustained glutamate release (Srivastava
667 et al., 2022). Additional related mechanisms that we did not directly investigate here may
668 contribute as well. For example, presynaptic resting potential has a strong effect on steady-state
669 vesicle release and thus stimulus-evoked release dynamics. Exocytosis that occurs when
670 bipolar cells rest at voltages near release threshold can lead to a depletion of readily-releasable
671 vesicles that limits the amount of release that occurs upon further light-induced depolarizations
672 (Grimes et al., 2014; Jarsky et al., 2011; Oesch and Diamond, 2011). Thus, an initial phasic
673 component of release can be reduced by depolarized resting potentials whereas hyperpolarized
674 potentials can facilitate greater occupancy of vesicles in the releasable pool, which can enhance
675 response transience. Bipolar subtype-dependent differences in release threshold due to
676 differential Ca^{2+} channel expression/regulation (Pangrsic et al., 2018) and/or coupling between
677 Ca^{2+} channel activity and vesicle release (Burrone et al., 2002; Burrone and Lagnado, 2000)
678 could also impact release dynamics. Several aspects of excitatory synaptic currents in the two
679 RGC types we studied here are consistent with a situation in which bipolar cell inputs to ON-T
680 RGCs have a higher threshold for glutamate release compared to those at ON-S RGCs; ON-T
681 RGCs receive less spontaneous excitatory synaptic input than ON-S RGCs (Kuo et al., 2016)
682 and stimulus-evoked EPSCs are slower, sparser and more biased towards larger amplitude
683 events in ON-T RGCs compared to those in ON-S RGCs (Fig. 2, Fig. S1B). Further

684 investigation will be required to determine whether this is due to differences in axon terminal
685 resting potential and/or other presynaptic factors. We did not find evidence for subtype-specific
686 differences in resting membrane potential among type 5i, type 6 and type 7 bipolar cells, but our
687 somatic voltage recordings likely have limited ability to resolve small voltage differences at the
688 bipolar cell axon terminals.
689
690 Our results do not rule out additional roles for postsynaptic mechanisms in establishing transient
691 versus sustained RGC spike output. For example, delayed amacrine cell-mediated inhibitory
692 synaptic input to RGC dendrites could truncate spiking responses (Nirenberg and Meister,
693 1997). RGC cell-intrinsic mechanisms, such as RGC subtype-specific differences in voltage-
694 gated Na^+ channel properties and/or expression pattern could also contribute to distinct
695 response kinetics (Brombas et al., 2022; Chang et al., 2023; Werginz et al., 2020). While a
696 combination of pre- and postsynaptic factors may ultimately act in concert to generate transient
697 versus sustained RGC spike output (Warwick et al., 2018; Werginz et al., 2020), our results
698 establish a fundamental role for bipolar cell synapses in the segregation of visual input into
699 kinetically distinct channels in ON pathways of the retina.
700
701 ***Materials and Methods***
702
703 *Animals*
704
705 Experiments used 5- to 15-week-old wild-type, *Grm6-tdTomato* (Morgan et al., 2011), *Gus8.4-*
706 *EGFP* (Huang et al., 1999), *Gjd2-EGFP*, or Kcng4-Cre (Duan et al., 2014) transgenic mice.
707 Transgenic mouse strains were backcrossed into the same genetic background as wild-type
708 mice (C57BL/6J; Jackson Laboratory). Animal care and handling followed procedures approved
709 by the Institutional Animal Care and Use Committee of the University of Washington or the
710 University of Victoria Animal Care Committee.
711
712 *Tissue preparation*
713
714 Retinal tissue was prepared for physiological recordings as previously described (Kuo et al.,
715 2016; Srivastava et al., 2022). Briefly, mice were killed by cervical dislocation or decapitation
716 and retinas were dissected from both eyes in oxygenated (95% O_2, 5% CO_2), bicarbonate-
717 buffered Ames' (Sigma) or artificial cerebrospinal fluid (ACSF) solution and either flat-mounted
718 with the vitreal surface facing up onto a poly-D-lysine coated glass coverslip (Corning) (RGC
719 patch-clamp recordings and iGluSnFR imaging) or sliced in an orientation perpendicular to the
720 flat-mount plane using a vibratome (200 µm slice thickness; bipolar cell recordings) before being
721 transferred to an upright 2P fluorescence microscope. ACSF contained (in mM): 125 NaCl, 2.5
722 KCl, 1.2 $CaCl_2$, 1.5 $MgCl_2$, 1.25 NaH_2PO_4, 20 glucose, 0.5 L-glutamine, 0.1 sodium ascorbate,
723 and 26 $NaHCO_3$ (pH 7.4, 310mOsm/L). All experiments exclusively used tissue from ventral
724 retina.
725
726 *Electrophysiology*
727
728 During recordings, retinal tissue was continuously perfused (~6-8 mL/min) with oxygenated,
729 bicarbonate-buffered Ames' solution maintained at 30-34 ºC. In a subset of electrophysiological
730 recordings (Figs. 6C-F and S8), tissue was perfused with ACSF rather than Ames' solution.
731 Electrical signals were acquired at 10 kHz and low-pass filtered at 3 kHz using a Multiclamp
732 700B or Multiclamp 700A amplifier (Molecular Devices) and Symphony Data Acquisition
733 software (http://symphony-das.github.io). The somas of different ON bipolar cell subtypes were
734 targeted for gramicidin perforated-patch current-clamp recordings using 2P laser scanning

735 excitation (960nm) in retinal slices prepared from transgenic mouse lines in which bipolar cell
736 subtypes expressed fluorescent proteins. Tissue from *Grm6-tdTomato* mice, in which a sparse
737 subset of ON bipolar cell types (type 6, 7 and 8) express tdTomato was used to target
738 recordings to type 6 bipolar cells (Morgan et al., 2011; Schwartz et al., 2012). Type 7 bipolar
739 cells were targeted for recording in *Gus8.4-EGFP* mice, which express EGFP in a type 7 bipolar
740 cells and rod bipolar cells (Huang et al., 2003). Type 5i bipolar cells were targeted in retinas
741 from *Gjd2-EGFP* mice, which we found express EGFP selectively in these bipolar cells (Fig. S6)
742 as well as less robustly in an uncharacterized amacrine cell type (not shown). For bipolar cell
743 recordings, we minimized light exposure from the 2P laser by restricting scan regions to the
744 inner retina, away from photoreceptors, and by keeping laser exposure brief (<~30 sec/scan
745 region; <2 mW post-objective laser power) (Kuo et al., 2016). After identification of fluorescent
746 cell bodies, we acquired recordings using infrared differential interference contrast microscopy.
747 Bipolar recordings used an internal solution containing 123 mM K-aspartate, 10 mM KCl, 10 mM
748 HEPES, 1 mM $MgCl_2$, 1 mM $CaCl_2$, 2 mM EGTA, 4 mM Mg-ATP, 0.5 mM Tris-GTP, 100 µM
749 Alexa Fluor 594-hydrazide and 25-30 µg/mL gramicidin D (280 mOsm/L; pH 7.2). Pipettes (~7-9
750 Ω tip resistance) were front-filled with gramicidin-free internal solution to facilitate formation of
751 high resistance (>1 GΩ) seals between patch pipettes and the cell membrane. After seal
752 formation, series resistance (R_s) was monitored in voltage-clamp mode by applying a 10 mV
753 voltage step across the pipette tip. Experiments were initiated once R_s declined to <50 MΩ,
754 which typically took 20-30 min. During recordings, we occasionally confirmed the integrity of the
755 cell membrane under the recording electrode by monitoring Alexa Fluor 594 fluorescence using
756 2P excitation; if any dye was visible in the cell body, we abandoned the recording. No holding
757 current was applied during current-clamp recordings from bipolar cells. At the conclusion of
758 each bipolar cell recording, the membrane under the patch pipette was intentionally ruptured
759 and fluorescence images of Alexa Fluor 594-filled cells were acquired using 2P microscopy to
760 confirm bipolar cell subtype identities (Wässle et al., 2009).
761
762 RGC recordings were performed in a flat-mount preparation of the retina from wild-type mice or
763 *Gjd2-EGFP* transgenic mice following previously described methods (Kuo et al., 2016)
764 Excitatory synaptic currents were isolated in whole-cell voltage-clamp recordings by holding
765 RGCs near the reversal potential for Cl^-- mediated conductances (-68.5 mV). Patch pipettes
766 (2.5-4 MΩ) were filled with an internal solution containing (in mM): 105 Cs-methanesulfonate, 10
767 Tetraethylammonium-Cl, 20 HEPES, 10 EGTA, 2 QX-314, 5 Mg-ATP, 0.5 Tris-GTP (~280
768 mOsm; pH 7.2). Series resistance (<15 MΩ) was compensated by 70% using the amplifier
769 circuitry. Inhibitory receptor antagonists (SR-95531, TPMPA, strychnine) were obtained from
770 Tocris or Sigma Aldrich and added to the bath solution from concentrated aqueous stock
771 solutions.
772
773 *iGluSnFR expression and two-photon imaging*
774
775 Intravitreal injection of a cre-dependent viral plasmid (pAAV.hSyn.Flex.iGluSnFR.WPRE.SV40)
776 was performed into Kcng4-cre mice to selectively express the glutamate sensor, iGluSnFR, in
777 alpha RGCs, including ON-T and ON-S RGCs (Krieger et al., 2017). All injection procedures,
778 tissue preparations, and subsequent two-photon imaging were performed as previously
779 described in Srivastava et al., 2022. Briefly, for iGluSnFR imaging, the laser was tuned to 920
780 nm and all recordings were acquired at a frame rate of 58.25 Hz (256 x 256 pixels). In KCNG4-
781 Cre mice, ON-S alpha RGCs were first identified by their spiking properties using extracellular
782 cell-attached recordings. To identify the dendrites of ON-S RGCs, cells were filled with
783 sulphorhodamine 101. ON-T RGC dendrites were then recorded at the same location but
784 deeper into the retina (Krieger et al., 2017).
785

786 *Visual stimulation*
787
788 Visual stimuli were presented from a photopic mean background illumination (~3,300 rhodopsin
789 isomerizations per rod per second (R*/rod/s)) to focus specifically on cone-mediated signaling
790 (Grimes et al., 2018). Visual stimuli for electrophysiological recordings were generated using
791 Stage Visual Stimulation Software (http://stage-vss.github.io). For all electrophysiological
792 recordings except those in Figs. 6C-F and S8, light stimuli consisted of a spatially uniform
793 circular spot (520 μm diameter) delivered from a LED (405 nm peak output; Hosfelt) that was
794 focused through the microscope substage condenser (Kuo et al., 2016). In the experiments
795 shown in Figs. 6C-F and S8, a Digital Light Processing (DLP) projector driven by a 405 nm LED
796 (Wintech Digital) was used to project spots of various sizes through the microscope objective
797 (Kuo et al., 2020). For iGluSnFR imaging (Fig. 5), background illuminance was kept around
798 1000 photons/μm^2/s. For experiments, static spots of different sizes were generated and
799 presented using StimGen software (https://github.com/benmurphybaum/StimGen). Stimuli were
800 presented via a DLP through the substage condenser focused onto the photoreceptor layer of
801 the retina. All visual stimuli were presented 4 s after the start of the recording for a duration of 2
802 s.
803
804 *Data analysis and statistics*
805
806 Spike triggered average (STA) waveforms (Fig. 1) and linear-nonlinear (LN) models of light-
807 driven RGC (Fig. 2) and bipolar cell (Fig.4) responses were derived from responses to randomly
808 fluctuating light stimuli (Gaussian distribution of light intensities with standard deviation = 50% of
809 mean intensity; 0-60 Hz bandwidth) as described previously (Chichilnisky, 2001; Kim and Rieke,
810 2001; Rieke, 2001). For LN model construction, the linear filter was calculated by computing the
811 cross-correlation of the light stimulus with the measured voltage (bipolar cell) or current (RGC)
812 response and dividing the result by the power spectrum of the stimulus. The static nonlinearity
813 was constructed from a point-by-point comparison of the predicted filter output with the
814 measured response and binning the result along the prediction axis. In almost all cases, the
815 linear filter had a biphasic shape with initial and secondary lobes that are opposite polarity. A
816 small number of bipolar cells had triphasic filters (Fig. S7). We quantified the kinetics of each
817 STA or linear filter by measuring the time at which the STA/filter waveform crossed zero ("zero-
818 cross time"; e.g. Fig. 1C, left) between the first and second lobes of the filter (e.g. between peak
819 and trough of STA waveforms) and by calculating a biphasic index = |A| / |B|, where |B| is the
820 absolute peak amplitude of the initial lobe of the filter and |A| is the amplitude of the peak
821 amplitude of the secondary lobe (e.g. Fig. 2C, right). We quantified the kinetics of responses to
822 light step stimuli by calculating the time between light step onset and the peak amplitude
823 response ("time to peak"; e.g. Fig. 2E, left) and dividing the mean steady-state response
824 (calculated from the last 100 ms light step increment) by the peak amplitude initial response at
825 step onset (and multiplying by 100) (e.g. Fig. 2E, right). We note that alternative measures of
826 step response or linear filter kinetics than those presented in Fig. 4 were also not statistically
827 different between bipolar cell subtypes (not shown). Statistical tests were performed using
828 MATLAB (Mathworks) or Igor Pro (WaveMetrics) software.
829
830 *Biolistic transfection*
831
832 DNA plasmids encoding mTFP1-myc (24 μg) and PSD95-mCherry (12 μg) under the control of
833 the cytomegalovirus (CMV) promoter were coated onto gold particles (1.6 μm diameter, 12.5
834 mg, Bio-Rad). Using a Helios gene gun (40 psi, Bio-Rad), these particles were then delivered to
835 retinal ganglion cells in whole-mount retinas. Subsequently, the transfected retinas were
836 incubated overnight in mACSF within a humid, oxygenated chamber maintained at 33°C.

837 *Immunohistochemistry*
838
839 Retinal sections (60 µm thick) were prepared using a vibratome (Leica) from retinal whole
840 mount retinas of *Gjd2-EGFP* mice. Both whole mount retinas and retinal sections were fixed in
841 4% PFA for 30 minutes. Retinal sections were embedded in low melting point agarose (Sigma-
842 Aldrich). Retinal tissues were first incubated with blocking solution (5% normal donkey serum,
843 0.5% Triton-X100 in PBS, Sigma-Aldrich) for 2 hours at 4°C, then incubated overnight at 4°C
844 with primary antibodies dissolved in blocking solution. Excess primary antibody was rinsed 3x10
845 minutes with PBS, then sections were incubated for 2 hours with secondary antibodies
846 dissolved in PBS. Excess secondary antibody was rinsed 3x10 minutes with PBS and sections
847 were mounted on standard microscopy glass slides using Vectashield mounting medium
848 (Vector). Primary antibody used in the study were: goat anti-ChAT diluted 1:1000 Chemicon
849 AB144P, mouse anti-CaBP5 diluted 1:1000 courtesy of Dr. Haeseleer, mouse anti-myc diluted
850 at 1:1000, chicken anti-GFP diluted at 1:1000. Secondary antibody were donkey anti-goat IgG
851 Dylight-568 diluted 1:1000, donkey anti-mouse Dylight-647 diluted 1:1000, donkey anti-mouse
852 Dylight-405 diluted at 1:1000 , donkey anti-chicken Alexa 488, the nuclear dye TOPRO3 (diluted
853 1:200, Thermo-Fisher).
854
855 *Near-infrared branding (NIRB) and serial block face scanning electron microscopy (SBFSEM)*
856
857 Two neighboring ON-T RGCs were physiologically identified in *Gjd2-EGFP* mice. After
858 identifying ON-T RGCs via their characteristic step-evoked extracellular spike response (e.g.
859 Figure 1B), they were filled with Alexa 488 or Alexa 555. Dendritic arbors and T5i-BC axonal
860 arbors were imaged using a confocal microscope. The retina was then fixed with 4%
861 glutaraldehyde for 30 minutes at room temperature (RT). The retina was washed with 0.1M Na+
862 Cacodylate buffer for three times and flat-mounted with 0.1M Na+ Cacodylate buffer. To
863 relocate the two RGCs under electron microscopy, we applied the near-infrared branding
864 (NIRB) technique previously published to burn fiducial markers in the retina (Bishop et al.). After
865 NIRBing, the retina tissue was unmounted and fixed in 4% glutaraldehyde overnight. The retina
866 was processed for SBFSEM subsequently according to the protocol described previously (Glumi
867 paper). Briefly, the tissue was initially treated with reduced osmium for 1 hour in the refrigerator.
868 Subsequently, after washing with double-distilled H2O (ddH2O), the tissue was placed in a
869 freshly prepared thiocarbohydrazide solution for 20 minutes at RT. Following another round of
870 ddH2O rinsing, the tissue was incubated in 2% osmium tetroxide for 30 minutes at RT. After
871 rinsing, the sample was incubated in 1% uranyl acetate at 4°C overnight. Post-wash, the tissue
872 was stained with Walton's lead aspartate for 30 minutes at 60°C. Following another wash, the
873 retinal piece underwent dehydration using a graded alcohol series (20%, 50%, 70%, 90%,
874 100%, 100%), each step lasting 5 minutes, followed by two changes of 100% propylene oxide at
875 RT for 10 minutes each. Finally, the tissue was embedded in Epon. The resulting block was
876 then trimmed and mounted in the SBEM microscope (GATAN/Zeiss SIGMA, 3View), and image
877 stacks were acquired at a voxel size of 5 x 5 x 50 nm.
878
879
880

881 ***References***
882

883 Angueyra JM, Rieke F. 2013. Origin and effect of phototransduction noise in primate cone
884 photoreceptors. *Nat Neurosci* **16**:1692–1700. doi:10.1038/nn.3534
885 Asari H, Meister M. 2014. The projective field of retinal bipolar cells and its modulation by
886 visual context. *Neuron* **81**:641–652. doi:10.1016/j.neuron.2013.11.029
887 Asari H, Meister M. 2012. Divergence of visual channels in the inner retina. *Nat Neurosci*
888 **15**:1581–1589. doi:10.1038/nn.3241
889 Awatramani GB, Slaughter MM. 2000. Origin of transient and sustained responses in ganglion
890 cells of the retina. *J Neurosci* **20**:7087–7095. doi:10.1523/JNEUROSCI.20-18-07087.2000
891 Baden T, Berens P, Bethge M, Euler T. 2013. Spikes in mammalian bipolar cells support
892 temporal layering of the inner retina. *Curr Biol* **23**:48–52. doi:10.1016/j.cub.2012.11.006
893 Baden T, Berens P, Franke K, Román Rosón M, Bethge M, Euler T. 2016. The functional diversity
894 of retinal ganglion cells in the mouse. *Nature* **529**:345–350. doi:10.1038/nature16468
895 Bae JA, Mu S, Kim JS, Turner NL, Tartavull I, Kemnitz N, Jordan CS, Norton AD, Silversmith WM,
896 Prentki R, Sorek M, David C, Jones DL, Bland D, Sterling ALR, Park J, Briggman KL, Seung
897 HS, Eyewirers. 2018. Digital Museum of Retinal Ganglion Cells with Dense Anatomy and
898 Physiology. *Cell* **173**:1293-1306.e19. doi:10.1016/j.cell.2018.04.040
899 Bishop D, Nikić I, Brinkoetter M, Knecht S, Potz S, Kerschensteiner M, Misgeld T. 2011. Near-
900 infrared branding efficiently correlates light and electron microscopy. *Nat Methods*
901 **8**:568–570. doi:10.1038/nmeth.1622
902 Brombas A, Zhou X, Williams SR. 2022. Light-evoked dendritic spikes in sustained but not
903 transient rabbit retinal ganglion cells. *Neuron* **110**:2802-2814.e3.
904 doi:10.1016/j.neuron.2022.06.009
905 Burrone J, Lagnado L. 2000. Synaptic depression and the kinetics of exocytosis in retinal bipolar
906 cells. *J Neurosci* **20**:568–578. doi:10.1523/JNEUROSCI.20-02-00568.2000
907 Burrone J, Neves G, Gomis A, Cooke A, Lagnado L. 2002. Endogenous calcium buffers regulate
908 fast exocytosis in the synaptic terminal of retinal bipolar cells. *Neuron* **33**:101–112.
909 doi:10.1016/s0896-6273(01)00565-7
910 Cafaro J, Rieke F. 2013. Regulation of spatial selectivity by crossover inhibition. *J Neurosci*
911 **33**:6310–6320. doi:10.1523/JNEUROSCI.4964-12.2013
912 Cangiano L, Asteriti S, Cervetto L, Gargini C. 2012. The photovoltage of rods and cones in the
913 dark-adapted mouse retina. *J Physiol* **590**:3841–3855. doi:10.1113/jphysiol.2011.226878
914 Chang L, Ran Y, Yang M, Auferkorte O, Butz E, Hüser L, Haverkamp S, Euler T, Schubert T. 2023.
915 Spike desensitisation as a mechanism for high-contrast selectivity in retinal ganglion
916 cells. *Front Cell Neurosci* **17**:1337768. doi:10.3389/fncel.2023.1337768
917 Chichilnisky EJ. 2001. A simple white noise analysis of neuronal light responses. *Network*
918 **12**:199–213.
919 Cleland BG, Levick WR, Sanderson KJ. 1973. Properties of sustained and transient ganglion cells
920 in the cat retina. *J Physiol* **228**:649–680. doi:10.1113/jphysiol.1973.sp010105
921 Cohen E, Sterling P. 1990. Demonstration of cell types among cone bipolar neurons of cat
922 retina. *Philos Trans R Soc Lond B Biol Sci* **330**:305–321. doi:10.1098/rstb.1990.0201
923 Demb JB, Singer JH. 2012. Intrinsic properties and functional circuitry of the AII amacrine cell.
924 *Vis Neurosci* **29**:51–60. doi:10.1017/S0952523811000368

925 Diamond JS. 2017. Inhibitory Interneurons in the Retina: Types, Circuitry, and Function. *Annu*
926 *Rev Vis Sci* **3**:1–24. doi:10.1146/annurev-vision-102016-061345
927 Ding H, Smith RG, Poleg-Polsky A, Diamond JS, Briggman KL. 2016. Species-specific wiring for
928 direction selectivity in the mammalian retina. *Nature* **535**:105–110.
929 doi:10.1038/nature18609
930 Dowling JE, Boycott BB. 1966. Organization of the primate retina: electron microscopy. *Proc R*
931 *Soc Lond B Biol Sci* **166**:80–111. doi:10.1098/rspb.1966.0086
932 Duan X, Krishnaswamy A, De la Huerta I, Sanes JR. 2014. Type II cadherins guide assembly of a
933 direction-selective retinal circuit. *Cell* **158**:793–807. doi:10.1016/j.cell.2014.06.047
934 Euler T, Haverkamp S, Schubert T, Baden T. 2014. Retinal bipolar cells: elementary building
935 blocks of vision. *Nat Rev Neurosci* **15**:507–519. doi:10.1038/nrn3783
936 Euler T, Masland RH. 2000. Light-evoked responses of bipolar cells in a mammalian retina. *J*
937 *Neurophysiol* **83**:1817–1829. doi:10.1152/jn.2000.83.4.1817
938 Franke K, Berens P, Schubert T, Bethge M, Euler T, Baden T. 2017. Inhibition decorrelates visual
939 feature representations in the inner retina. *Nature* **542**:439–444.
940 doi:10.1038/nature21394
941 Ghosh KK, Bujan S, Haverkamp S, Feigenspan A, Wässle H. 2004. Types of bipolar cells in the
942 mouse retina. *J Comp Neurol* **469**:70–82. doi:10.1002/cne.10985
943 Goetz J, Jessen ZF, Jacobi A, Mani A, Cooler S, Greer D, Kadri S, Segal J, Shekhar K, Sanes JR,
944 Schwartz GW. 2022. Unified classification of mouse retinal ganglion cells using function,
945 morphology, and gene expression. *Cell Rep* **40**:111040.
946 doi:10.1016/j.celrep.2022.111040
947 Gollisch T, Meister M. 2010. Eye smarter than scientists believed: neural computations in
948 circuits of the retina. *Neuron* **65**:150–164. doi:10.1016/j.neuron.2009.12.009
949 Greene MJ, Kim JS, Seung HS, EyeWirers. 2016. Analogous Convergence of Sustained and
950 Transient Inputs in Parallel On and Off Pathways for Retinal Motion Computation. *Cell*
951 *Rep* **14**:1892–1900. doi:10.1016/j.celrep.2016.02.001
952 Grimes WN, Baudin J, Azevedo AW, Rieke F. 2018. Range, routing and kinetics of rod signaling in
953 primate retina. *Elife* **7**:e38281. doi:10.7554/eLife.38281
954 Grimes WN, Schwartz GW, Rieke F. 2014. The synaptic and circuit mechanisms underlying a
955 change in spatial encoding in the retina. *Neuron* **82**:460–473.
956 doi:10.1016/j.neuron.2014.02.037
957 Hellmer CB, Zhou Y, Fyk-Kolodziej B, Hu Z, Ichinose T. 2016. Morphological and physiological
958 analysis of type-5 and other bipolar cells in the Mouse Retina. *Neuroscience* **315**:246–
959 258. doi:10.1016/j.neuroscience.2015.12.016
960 Helmstaedter M, Briggman KL, Turaga SC, Jain V, Seung HS, Denk W. 2013. Connectomic
961 reconstruction of the inner plexiform layer in the mouse retina. *Nature* **500**:168–174.
962 doi:10.1038/nature12346
963 Huang L, Max M, Margolskee RF, Su H, Masland RH, Euler T. 2003. G protein subunit G gamma
964 13 is coexpressed with G alpha o, G beta 3, and G beta 4 in retinal ON bipolar cells. *J*
965 *Comp Neurol* **455**:1–10. doi:10.1002/cne.10396
966 Huang L, Shanker YG, Dubauskaite J, Zheng JZ, Yan W, Rosenzweig S, Spielman AI, Max M,
967 Margolskee RF. 1999. Ggamma13 colocalizes with gustducin in taste receptor cells and

968 mediates IP3 responses to bitter denatonium. *Nat Neurosci* **2**:1055–1062.
969 doi:10.1038/15981
970 Ichinose T, Fyk-Kolodziej B, Cohn J. 2014. Roles of ON cone bipolar cell subtypes in temporal
971 coding in the mouse retina. *J Neurosci* **34**:8761–8771. doi:10.1523/JNEUROSCI.3965-
972 13.2014
973 Ichinose T, Hellmer CB. 2016. Differential signalling and glutamate receptor compositions in the
974 OFF bipolar cell types in the mouse retina. *J Physiol* **594**:883–894. doi:10.1113/JP271458
975 Ikeda H, Wright MJ. 1972. Receptive field organization of "sustained" and "transient" retinal
976 ganglion cells which subserve different function roles. *J Physiol* **227**:769–800.
977 doi:10.1113/jphysiol.1972.sp010058
978 Jarsky T, Cembrowski M, Logan SM, Kath WL, Riecke H, Demb JB, Singer JH. 2011. A Synaptic
979 Mechanism for Retinal Adaptation to Luminance and Contrast. *J Neurosci* **31**:11003–
980 11015. doi:10.1523/JNEUROSCI.2631-11.2011
981 Ke J-B, Wang YV, Borghuis BG, Cembrowski MS, Riecke H, Kath WL, Demb JB, Singer JH. 2014.
982 Adaptation to background light enables contrast coding at rod bipolar cell synapses.
983 *Neuron* **81**:388–401. doi:10.1016/j.neuron.2013.10.054
984 Kerschensteiner D. 2022. Feature Detection by Retinal Ganglion Cells. *Annu Rev Vis Sci* **8**:135–
985 169. doi:10.1146/annurev-vision-100419-112009
986 Kim KJ, Rieke F. 2001. Temporal contrast adaptation in the input and output signals of
987 salamander retinal ganglion cells. *J Neurosci* **21**:287–299. doi:10.1523/JNEUROSCI.21-
988 01-00287.2001
989 Krieger B, Qiao M, Rousso DL, Sanes JR, Meister M. 2017. Four alpha ganglion cell types in
990 mouse retina: Function, structure, and molecular signatures. *PLoS One* **12**:e0180091.
991 doi:10.1371/journal.pone.0180091
992 Kuo SP, Chiang P-P, Nippert AR, Newman EA. 2020. Spatial Organization and Dynamics of the
993 Extracellular Space in the Mouse Retina. *J Neurosci* **40**:7785–7794.
994 doi:10.1523/JNEUROSCI.1717-20.2020
995 Kuo SP, Schwartz GW, Rieke F. 2016. Nonlinear Spatiotemporal Integration by Electrical and
996 Chemical Synapses in the Retina. *Neuron* **90**:320–332.
997 doi:10.1016/j.neuron.2016.03.012
998 Lagnado L, Schmitz F. 2015. Ribbon Synapses and Visual Processing in the Retina. *Annu Rev Vis*
999 *Sci* **1**:235–262. doi:10.1146/annurev-vision-082114-035709
1000 Marc RE, Anderson JR, Jones BW, Sigulinsky CL, Lauritzen JS. 2014. The AII amacrine cell
1001 connectome: a dense network hub. *Front Neural Circuits* **8**:104.
1002 doi:10.3389/fncir.2014.00104
1003 Margolis DJ, Gartland AJ, Euler T, Detwiler PB. 2010. Dendritic Calcium Signaling in ON and OFF
1004 Mouse Retinal Ganglion Cells. *J Neurosci* **30**:7127–7138. doi:10.1523/JNEUROSCI.5694-
1005 09.2010
1006 Masland RH. 2012. The Neuronal Organization of the Retina. *Neuron* **76**:266–280.
1007 doi:10.1016/j.neuron.2012.10.002
1008 McGuire BA, Stevens JK, Sterling P. 1984. Microcircuitry of bipolar cells in cat retina. *J Neurosci*
1009 **4**:2920–2938. doi:10.1523/JNEUROSCI.04-12-02920.1984

1010 Mennerick S, Matthews G. 1996. Ultrafast exocytosis elicited by calcium current in synaptic
1011 terminals of retinal bipolar neurons. *Neuron* **17**:1241–1249. doi:10.1016/s0896-
1012 6273(00)80254-8
1013 Morgan JL, Soto F, Wong ROL, Kerschensteiner D. 2011. Development of cell type-specific
1014 connectivity patterns of converging excitatory axons in the retina. *Neuron* **71**:1014–
1015 1021. doi:10.1016/j.neuron.2011.08.025
1016 Neves G, Lagnado L. 1999. The kinetics of exocytosis and endocytosis in the synaptic terminal of
1017 goldfish retinal bipolar cells. *J Physiol* **515 (Pt 1)**:181–202. doi:10.1111/j.1469-
1018 7793.1999.181ad.x
1019 Nirenberg S, Meister M. 1997. The light response of retinal ganglion cells is truncated by a
1020 displaced amacrine circuit. *Neuron* **18**:637–650. doi:10.1016/s0896-6273(00)80304-9
1021 Oesch NW, Diamond JS. 2011. Ribbon synapses compute temporal contrast and encode
1022 luminance in retinal rod bipolar cells. *Nat Neurosci* **14**:1555–1561. doi:10.1038/nn.2945
1023 Pangrsic T, Singer JH, Koschak A. 2018. Voltage-Gated Calcium Channels: Key Players in Sensory
1024 Coding in the Retina and the Inner Ear. *Physiol Rev* **98**:2063–2096.
1025 doi:10.1152/physrev.00030.2017
1026 Puthussery T, Venkataramani S, Gayet-Primo J, Smith RG, Taylor WR. 2013. NaV1.1 channels in
1027 axon initial segments of bipolar cells augment input to magnocellular visual pathways in
1028 the primate retina. *J Neurosci* **33**:16045–16059. doi:10.1523/JNEUROSCI.1249-13.2013
1029 Ran Y, Huang Z, Baden T, Schubert T, Baayen H, Berens P, Franke K, Euler T. 2020. Type-specific
1030 dendritic integration in mouse retinal ganglion cells. *Nat Commun* **11**:2101.
1031 doi:10.1038/s41467-020-15867-9
1032 Rieke F. 2001. Temporal contrast adaptation in salamander bipolar cells. *J Neurosci* **21**:9445–
1033 9454.
1034 Rodieck RW. 1991. The density recovery profile: a method for the analysis of points in the plane
1035 applicable to retinal studies. *Vis Neurosci* **6**:95–111. doi:10.1017/s095252380001049x
1036 Roska B, Werblin F. 2001. Vertical interactions across ten parallel, stacked representations in
1037 the mammalian retina. *Nature* **410**:583–587. doi:10.1038/35069068
1038 Sabbah S, Papendorp C, Koplas E, Beltoja M, Etebari C, Gunesch AN, Carrete L, Kim MT, Manoff
1039 G, Bhatia-Lin A, Zhao T, Schreck D, Dowling H, Briggman KL, Berson DM. 2018. Synaptic
1040 circuits for irradiance coding by intrinsically photosensitive retinal ganglion cells
1041 (preprint). Neuroscience. doi:10.1101/442954
1042 Sagdullaev BT, McCall MA, Lukasiewicz PD. 2006. Presynaptic inhibition modulates spillover,
1043 creating distinct dynamic response ranges of sensory output. *Neuron* **50**:923–935.
1044 doi:10.1016/j.neuron.2006.05.015
1045 Saszik S, DeVries SH. 2012. A mammalian retinal bipolar cell uses both graded changes in
1046 membrane voltage and all-or-nothing Na+ spikes to encode light. *J Neurosci* **32**:297–307.
1047 doi:10.1523/JNEUROSCI.2739-08.2012
1048 Schwartz GW, Okawa H, Dunn FA, Morgan JL, Kerschensteiner D, Wong RO, Rieke F. 2012. The
1049 spatial structure of a nonlinear receptive field. *Nat Neurosci* **15**:1572–1580.
1050 doi:10.1038/nn.3225
1051 Shekhar K, Lapan SW, Whitney IE, Tran NM, Macosko EZ, Kowalczyk M, Adiconis X, Levin JZ,
1052 Nemesh J, Goldman M, McCarroll SA, Cepko CL, Regev A, Sanes JR. 2016.

1053 Comprehensive Classification of Retinal Bipolar Neurons by Single-Cell Transcriptomics.
1054 *Cell* **166**:1308-1323.e30. doi:10.1016/j.cell.2016.07.054
1055 Sigulinsky CL, Anderson JR, Kerzner E, Rapp CN, Pfeiffer RL, Rodman TM, Emrich DP, Rapp KD,
1056 Nelson NT, Lauritzen JS, Meyer M, Marc RE, Jones BW. 2020. Network Architecture of
1057 Gap Junctional Coupling among Parallel Processing Channels in the Mammalian Retina. *J*
1058 *Neurosci* **40**:4483–4511. doi:10.1523/JNEUROSCI.1810-19.2020
1059 Singer JH, Diamond JS. 2006. Vesicle depletion and synaptic depression at a mammalian ribbon
1060 synapse. *J Neurophysiol* **95**:3191–3198. doi:10.1152/jn.01309.2005
1061 Singer JH, Diamond JS. 2003. Sustained Ca2+ entry elicits transient postsynaptic currents at a
1062 retinal ribbon synapse. *J Neurosci* **23**:10923–10933. doi:10.1523/JNEUROSCI.23-34-
1063 10923.2003
1064 Slaughter MM, Miller RF. 1981. 2-amino-4-phosphonobutyric acid: a new pharmacological tool
1065 for retina research. *Science* **211**:182–185. doi:10.1126/science.6255566
1066 Srivastava P, de Rosenroll G, Matsumoto A, Michaels T, Turple Z, Jain V, Sethuramanujam S,
1067 Murphy-Baum BL, Yonehara K, Awatramani GB. 2022. Spatiotemporal properties of
1068 glutamate input support direction selectivity in the dendrites of retinal starburst
1069 amacrine cells. *Elife* **11**:e81533. doi:10.7554/eLife.81533
1070 Szikra T, Trenholm S, Drinnenberg A, Jüttner J, Raics Z, Farrow K, Biel M, Awatramani G, Clark
1071 DA, Sahel J-A, da Silveira RA, Roska B. 2014. Rods in daylight act as relay cells for cone-
1072 driven horizontal cell-mediated surround inhibition. *Nat Neurosci* **17**:1728–1735.
1073 doi:10.1038/nn.3852
1074 Taylor WR, Vaney DI. 2002. Diverse synaptic mechanisms generate direction selectivity in the
1075 rabbit retina. *J Neurosci* **22**:7712–7720.
1076 Tsukamoto Y, Omi N. 2017. Classification of Mouse Retinal Bipolar Cells: Type-Specific
1077 Connectivity with Special Reference to Rod-Driven AII Amacrine Pathways. *Front*
1078 *Neuroanat* **11**:92. doi:10.3389/fnana.2017.00092
1079 Vaney DI, Sivyer B, Taylor WR. 2012. Direction selectivity in the retina: symmetry and
1080 asymmetry in structure and function. *Nat Rev Neurosci* **13**:194–208.
1081 doi:10.1038/nrn3165
1082 Veruki ML, Hartveit E. 2002a. Electrical synapses mediate signal transmission in the rod
1083 pathway of the mammalian retina. *J Neurosci* **22**:10558–10566.
1084 doi:10.1523/JNEUROSCI.22-24-10558.2002
1085 Veruki ML, Hartveit E. 2002b. AII (Rod) amacrine cells form a network of electrically coupled
1086 interneurons in the mammalian retina. *Neuron* **33**:935–946. doi:10.1016/s0896-
1087 6273(02)00609-8
1088 von Gersdorff H, Matthews G. 1997. Depletion and replenishment of vesicle pools at a ribbon-
1089 type synaptic terminal. *J Neurosci* **17**:1919–1927. doi:10.1523/JNEUROSCI.17-06-
1090 01919.1997
1091 Warwick RA, Kaushansky N, Sarid N, Golan A, Rivlin-Etzion M. 2018. Inhomogeneous Encoding
1092 of the Visual Field in the Mouse Retina. *Curr Biol* **28**:655-665.e3.
1093 doi:10.1016/j.cub.2018.01.016
1094 Wässle H, Puller C, Müller F, Haverkamp S. 2009. Cone contacts, mosaics, and territories of
1095 bipolar cells in the mouse retina. *J Neurosci* **29**:106–117. doi:10.1523/JNEUROSCI.4442-
1096 08.2009

1097 Werblin FS. 1970. Response of retinal cells to moving spots: intracellular recording in Necturus
1098 maculosus. *J Neurophysiol* **33**:342–350. doi:10.1152/jn.1970.33.3.342
1099 Werginz P, Raghuram V, Fried SI. 2020. Tailoring of the axon initial segment shapes the
1100 conversion of synaptic inputs into spiking output in OFF-α T retinal ganglion cells. *Sci*
1101 *Adv* **6**:eabb6642. doi:10.1126/sciadv.abb6642
1102 Wienbar S, Schwartz GW. 2022. Differences in spike generation instead of synaptic inputs
1103 determine the feature selectivity of two retinal cell types. *Neuron* **110**:2110-2123.e4.
1104 doi:10.1016/j.neuron.2022.04.012
1105 Wu SM, Gao F, Maple BR. 2000. Functional architecture of synapses in the inner retina:
1106 segregation of visual signals by stratification of bipolar cell axon terminals. *J Neurosci*
1107 **20**:4462–4470. doi:10.1523/JNEUROSCI.20-12-04462.2000
1108 Yu W-Q, Swanstrom R, Sigulinsky CL, Ahlquist RM, Knecht S, Jones BW, Berson DM, Wong RO.
1109 2023. Distinctive synaptic structural motifs link excitatory retinal interneurons to diverse
1110 postsynaptic partner types. *Cell Rep* **42**:112006. doi:10.1016/j.celrep.2023.112006
1111 Zhang Y, Kim I-J, Sanes JR, Meister M. 2012. The most numerous ganglion cell type of the
1112 mouse retina is a selective feature detector. *Proc Natl Acad Sci U S A* **109**:E2391-2398.
1113 doi:10.1073/pnas.1211547109
1114
1115

1116 ***Supplemental Information***
1117
1118

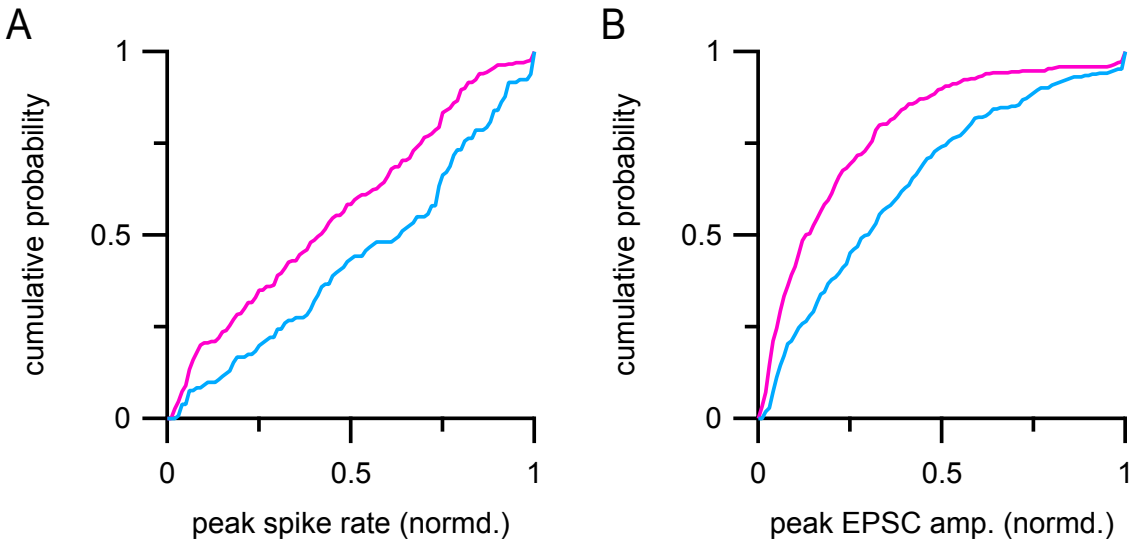

1119
1120
1121 ***Figure S1****. Noise-evoked responses are biased towards large amplitude events in ON-T*
1122 *compared to ON-S RGCs. (A) Spike event peak spike rate cumulative distributions for ON-T*
1123 *(magenta; n= 6 cells; 131 spike events) and ON-S RGC (cyan; n= 7 cells; 300 spike events).*
1124 *Firing rates from average responses to a repeated noise stimulus (see Fig. 1B-C) were*
1125 *normalized to the maximal firing rate in each cell before combining events across cells. (B)*
1126 *EPSC amplitude cumulative distributions for ON-T (n= 13 cells; 275 EPSCs) and ON-S (n= 10*
1127 *cells; 365 EPSCs) RGCs. Same stimulus and normalization procedure as in (A).*
1128

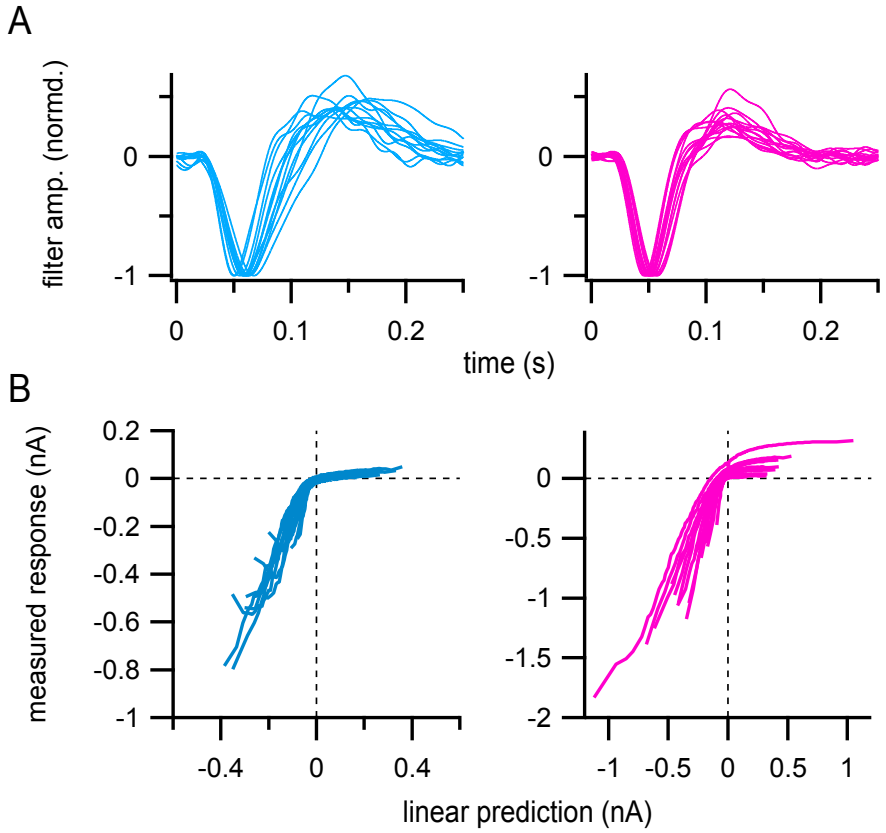

Figure S2. *Linear-nonlinear models of excitatory synaptic input to ON-T and ON-S RGCs. (A) Linear filters computed from responses to non-repeated noise stimulus presentation. Lines show filters from individual ON-T (cyan; n= 13) and ON-S (magenta; n= 15) RGCs. Filters were normalized to the peak amplitude of the primary inward component to facilitate visual comparison of temporal responses. Same cells as shown in average filters in Fig. 2B. (B) Nonlinearities derived by plotting the predicted response (convolution of linear filter and stimulus) against the measured excitatory currents for each RGC shown in (A). Linear predictions were calculated using non-normalized filters.*

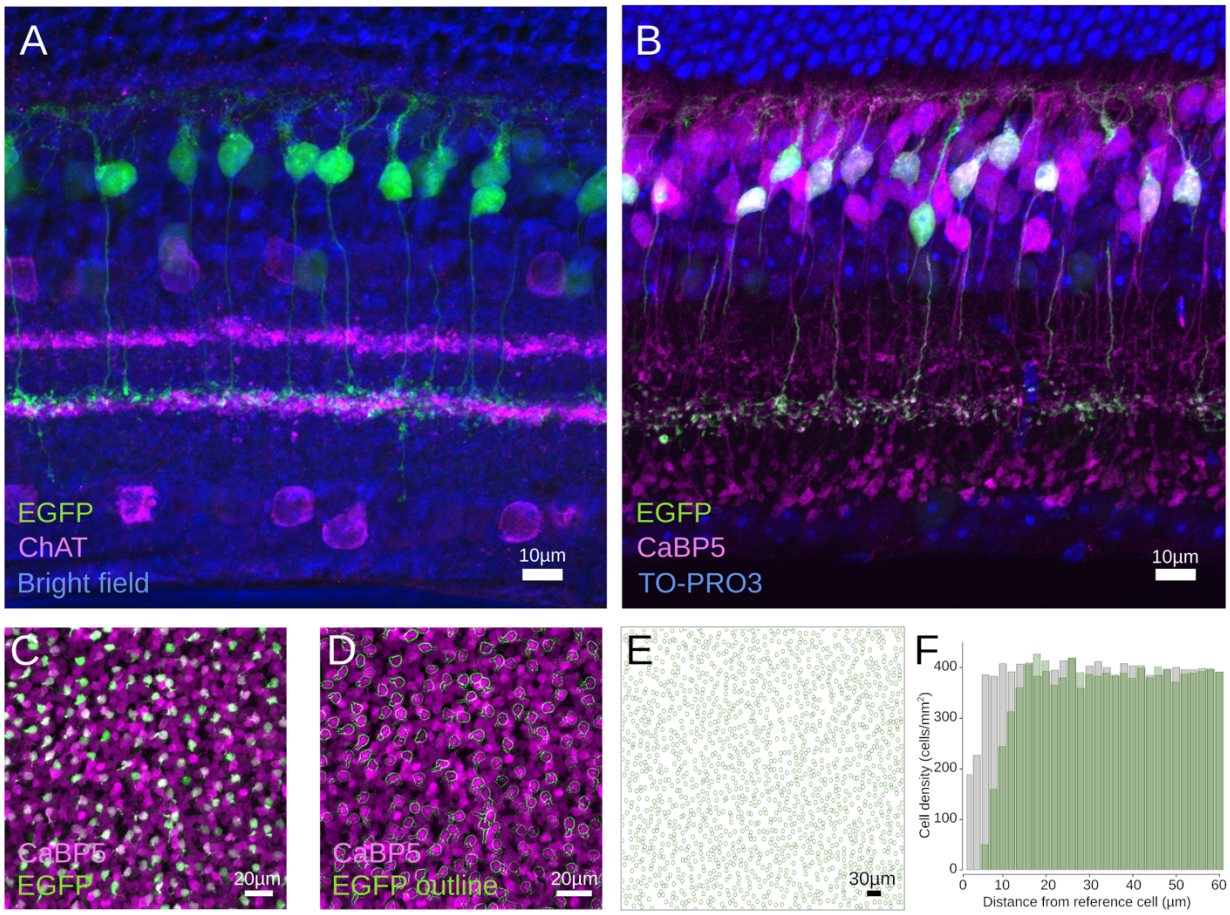

Figure S3. *Characterization of Gjd2-EGFP+ bipolar cells. (A) Vertical section of the Gjd2-EGFP mouse line showing EGFP positive bipolar cells axons (green) stratifying in the ON sublamina of the IPL, co-labeled with cholinergic amacrine cell (magenta, ChAT antibody). Transmitted light image of the retina in blue. (B) Vertical section of the Gjd2-EGFP mouse line showing EGFP positive bipolar cells (green) colocalized with the T5 marker CaBP5 (magenta). (C) En-face image of a whole mount retina from the GJD2 mouse line showing EGFP positive bipolar cells bodies (green) co-labeled with the T5 bipolar cell marker CaBP5 (magenta). (D) Same field as in (C) with cell bodies of EGFP positive bipolar cells outlined (green) by application of a digital edge outlining filter in ImageJ. (E) Position of cell body centroids for EGFP positive bipolar cells in a larger field of view (20X objective) outlined by green circles. (F) Density recovery profile analysis showing the density profile as a function of distance from the reference neuron for EGFP positive bipolar cells (green histograms) and for an equal amount of neurons randomly positioned in the same space (grey histograms) showing the presence of a characteristic exclusion distance for EGFP positive bipolar cells, hallmark of a retinal mosaic.*

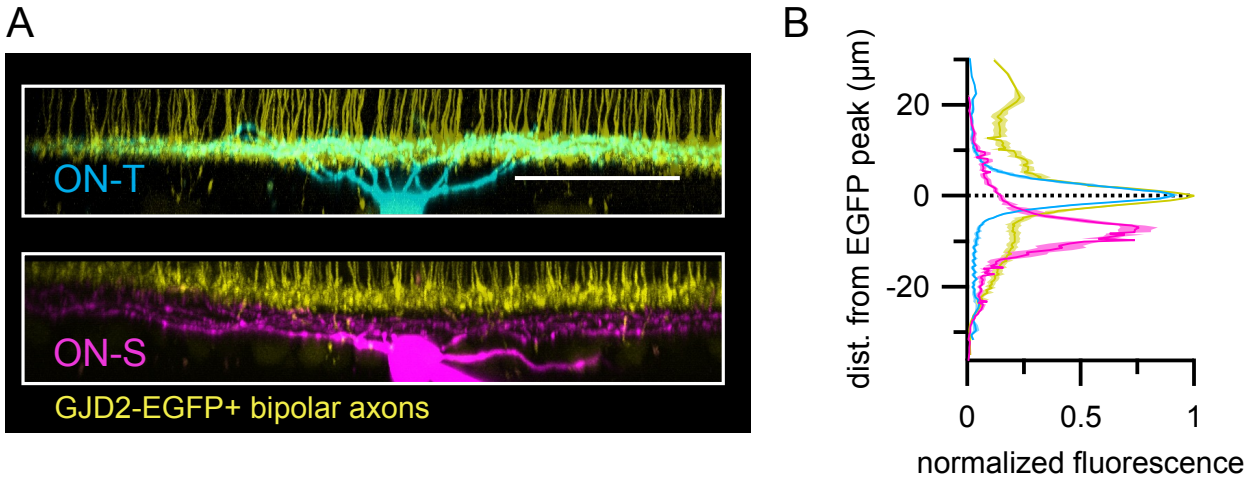

Figure S4. *ON-T and ON-S RGC dendrites ramify in distinct IPL sublaminae. (A) Side projections from 2P z-stack images of dye-filled RGCs (ON-T: top, cyan; ON-S: bottom, magenta) and EGFP signal (yellow) in retinas from Gjd2-EGFP mice. RGCs are same cells as shown in en face view in Fig. 1A (B) Quantification of fluorescence signals from dye filled RGCs in Gjd2-EGFP mouse retina as in (A). Colored lines and shaded areas show mean ± SEM fluorescence intensity with respect to distance from peak EGFP (yellow) fluorescence intensity (n= 6 ON-T, cyan and n= 4 ON-S, magenta, RGCs).*

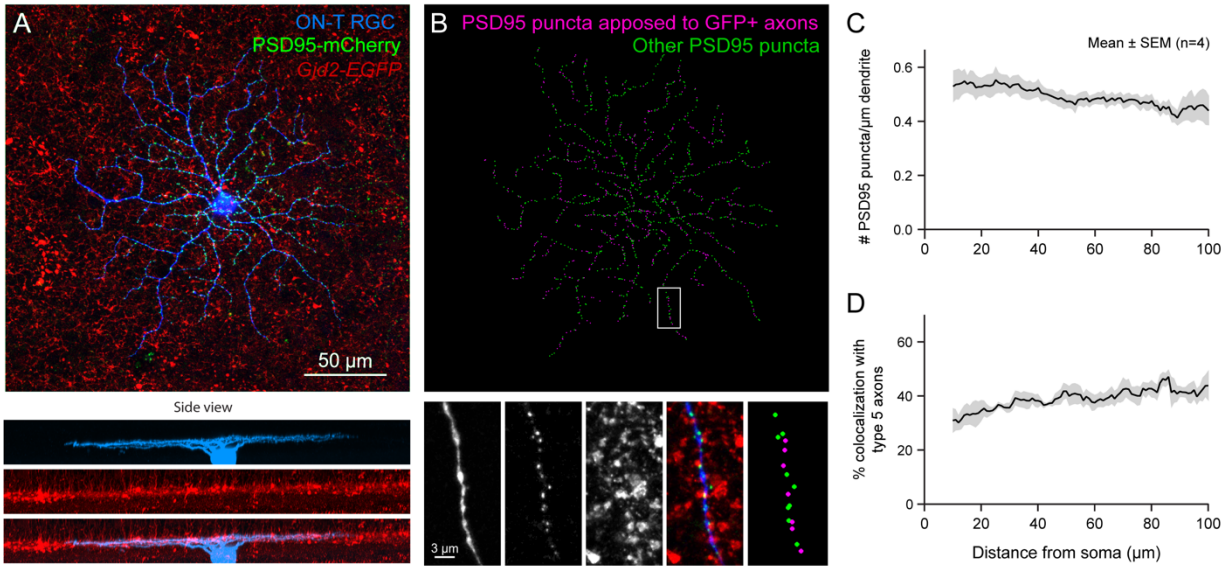

Figure S5. *Gjd2-EGFP+ type 5 bipolar cells provide ~40% of total synapses onto ON-T RGCs. (A) An example ON-T RGC biolistically labeled by Cerulean Fluorescent Protein (blue) and PSD95-mCherry (green) in retina from a Gjd2-EGFP (red) transgenic mouse. Top: en face view, Bottom: side views. (B) Top: Dot map of PSD95-mCherry apposed (magenta) or not apposed (green) to GFP+ BC axon terminals. Bottom: Magnified view of the raw images and the dot map for a segment of dendritic arbor in the while box. (C) Quantification of total excitatory synapse density across the dendritic arbor of ON-T RGCs. (D) Quantification of excitatory synapses in ON-T dendrites that are adjacent to GFP+ axon terminals.*

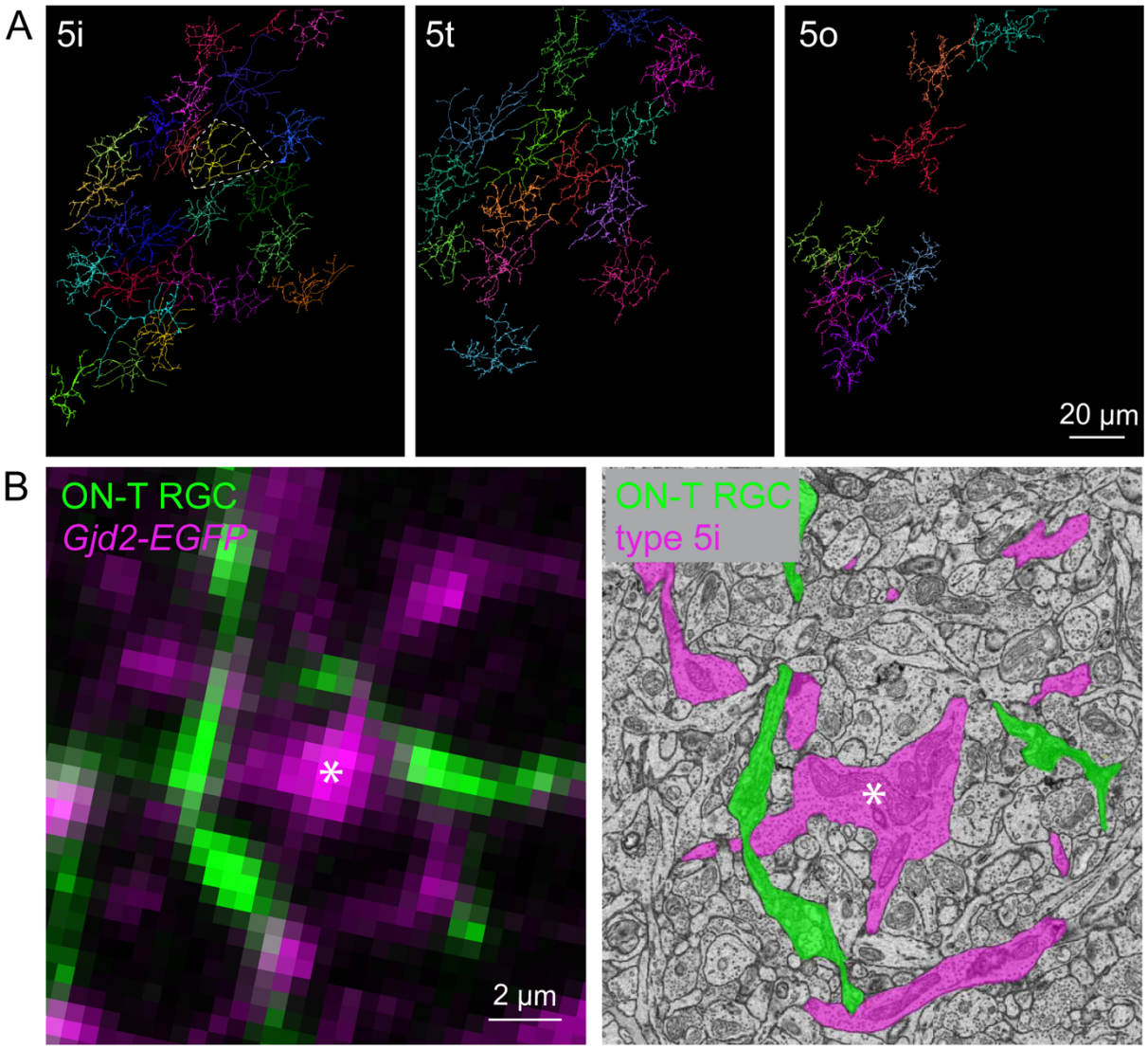

Figure S6. *Classification of three subtypes of type 5 bipolar cells. (A) Wholemount views of the axon terminals of type 5i, type 5t and type 5o bipolar cells in the SBFSEM volume in Fig. 3. The tiling of the space validates the categorization of the three subtypes of type 5 bipolar cells. (B) Identification of Gjd2-EGFP+ bipolar cells as type 5i bipolar cells, supported by correlated light (left) and electron (right) microscopy images. The reconstructed skeleton of the type 5i bipolar cell in (B) is delineated by dashed lines in (A).*

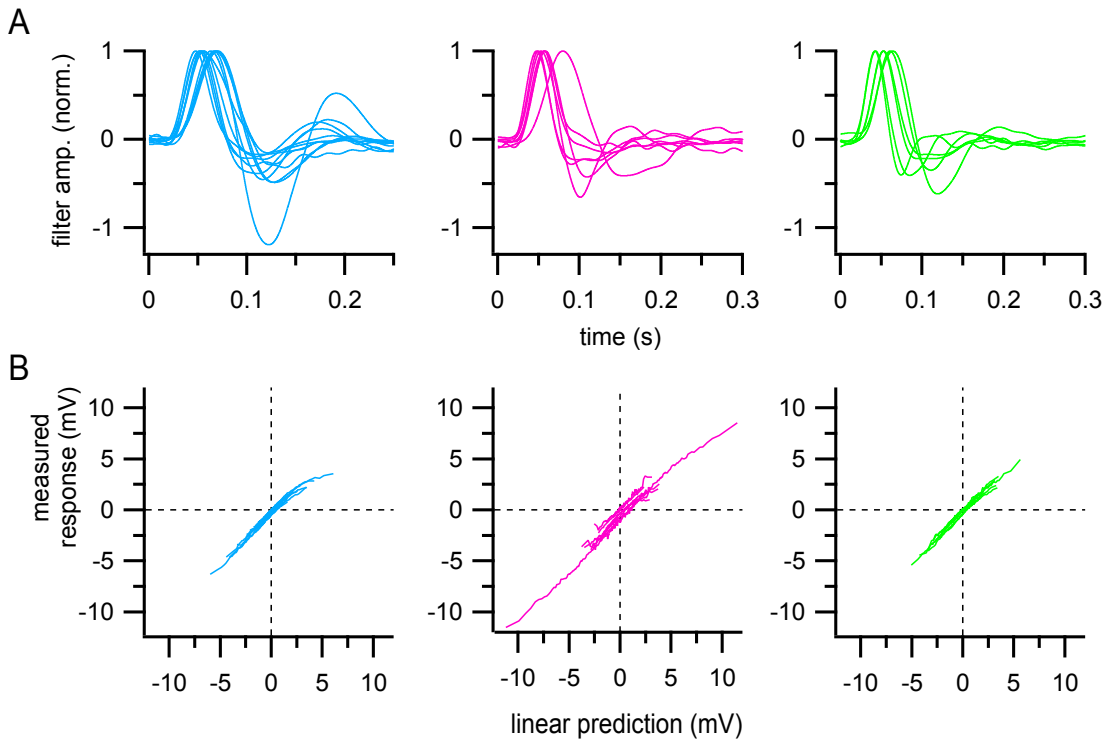

Figure S7. *Linear-nonlinear models of bipolar cell voltage responses. (A) Individual linear filters for all type 5i (cyan; n= 11), type 6 (magenta; n= 7), and type 7 (green; n=6) bipolar cells computed from responses to non-repeated noise stimulus presentation. Filters were normalized to the peak amplitude of the primary inward component to facilitate visual comparison of temporal responses. Same cells as shown in average filters in Fig. 4B. (B) Nonlinearities derived by plotting the predicted response (convolution of linear filter and stimulus) against the measured voltage response for each bipolar cell shown in (A). Linear predictions were calculated using non-normalized filters.*

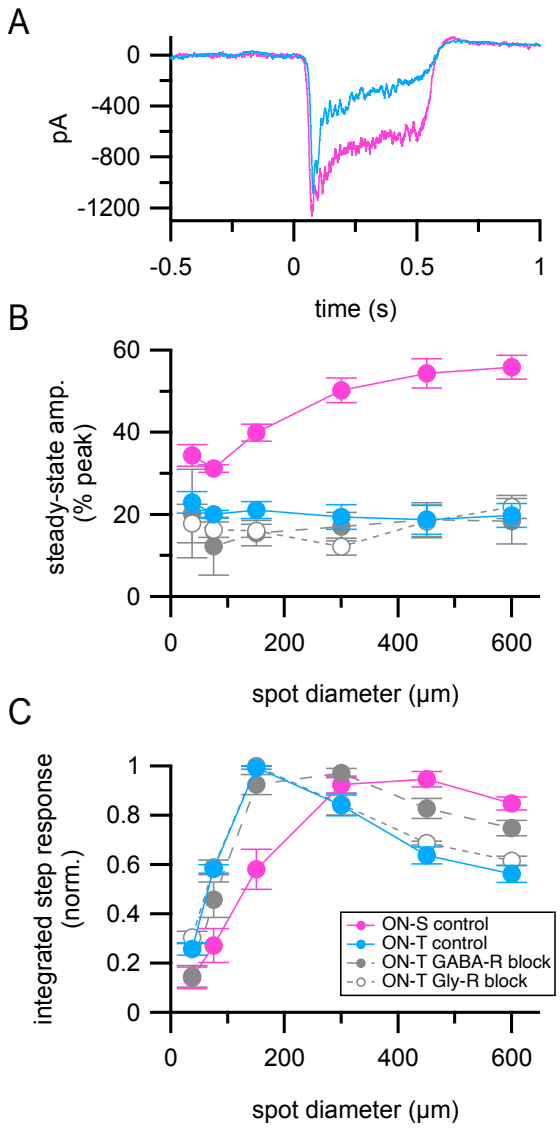

Figure S8*. Presynaptic inhibition does not affect response kinetics but does affect spatial integration for excitatory inputs to ON-T RGCs (A) Step-evoked (100% contrast, 300 μm spot diameter, 500 ms duration) excitatory synaptic currents in example ON-T (cyan) and ON-S RGCs measured in ACSF. Traces show mean responses to ten trials and are baseline subtracted to facilitate comparison. (B) Summary of light step-evoked steady-state response amplitude for different stimulus sizes measured in ACSF. Note that excitatory inputs in ON-T are more transient than those in ON-S RGCs across all stimulus sizes, but responses in both RGC types are more sustained than when measurements were performed using Ames' solution (compare to Fig. 2D-E). (C) Summary of total response, measured as the integrated excitatory current response during the light step, versus stimulus spot size. Responses were normalized to the maximal response in each cell prior to averaging. Excitation in ON-T RGCs is tuned to smaller spot sizes than in ON-S RGCs and this tuning relies in part on GABAergic inhibition. Symbols with error bars in (B) and (C) show mean ± SEM (ON-T control n = 12; ON-S control n = 6; ON-T GABA-R block n = 5; ON-T Gly-R block n = 5).*